

# Validated prediction of weld residual stresses in austenitic steel pipe girth welds before and after thermal ageing, Part 2: modelling and validation

Xiong, Q., Smith, M., Muransky, O. & Mathew, J.

Author post-print (accepted) deposited by Coventry University's Repository

**Original citation & hyperlink:**

Xiong, Q, Smith, M, Muransky, O & Mathew, J 2019, 'Validated prediction of weld residual stresses in austenitic steel pipe girth welds before and after thermal ageing, Part 2: modelling and validation' International Journal of Pressure Vessels and Piping, vol. 172, pp. 430-448.

<https://dx.doi.org/10.1016/j.ijpvp.2019.02.002>

DOI 10.1016/j.ijpvp.2019.02.002

ISSN 0308-0161

Publisher: Elsevier

**NOTICE: this is the author's version of a work that was accepted for publication in International Journal of Pressure Vessels and Piping. Changes resulting from the publishing process, such as peer review, editing, corrections, structural formatting, and other quality control mechanisms may not be reflected in this document. Changes may have been made to this work since it was submitted for publication. A definitive version was subsequently published in International Journal of Pressure Vessels and Piping, 172 (2019) DOI: 10.1016/j.ijpvp.2019.02.002**

© 2019, Elsevier. Licensed under the Creative Commons Attribution-NonCommercial-NoDerivatives 4.0 International <http://creativecommons.org/licenses/by-nc-nd/4.0/>

Copyright © and Moral Rights are retained by the author(s) and/ or other copyright owners. A copy can be downloaded for personal non-commercial research or study, without prior permission or charge. This item cannot be reproduced or quoted extensively from without first obtaining permission in writing from the copyright holder(s). The content must not be changed in any way or sold commercially in any format or medium without the formal permission of the copyright holders.

This document is the author's post-print version, incorporating any revisions agreed during the peer-review process. Some differences between the published version and this version may remain and you are advised to consult the published version if you wish to cite from it.

# Validated prediction of weld residual stresses in austenitic steel pipe girth welds before and after thermal ageing, Part 2: modelling and validation

Qingrong Xiong<sup>a</sup>, M C Smith<sup>a</sup>, O Muransky<sup>b,c</sup>, J Mathew<sup>d</sup>

a) The University of Manchester

b) Australian Science and Technology Organization (ANSTO), Sydney, NSW, Australia

c) School of Materials Science and Engineering, UNSW Sydney, Sydney, Australia

d) Faculty of Engineering and Computing, Coventry University, Priory Street, Coventry CV1 5FB, UK

## Abstract

An extensive finite element simulation campaign was undertaken to examine the complete manufacturing history and high temperature thermal ageing of thick-walled girth-welded austenitic steel pipes fabricated from Esshete 1250 austenitic steel. The simulations examined the impacts of prior quenching of pipe material, fabrication of closely adjacent welds, and axial restraint during welding. The simulations considered both simple isotropic and kinematic hardening behaviour, and a large matrix of Lemaitre-Chaboche mixed isotropic-kinematic hardening material constitutive models, with a focus on examining the most accurate evolutionary hardening behaviour for weld metal. High temperature (650°C) service exposure was modelled using an RCC-MR type creep model, and the sensitivity of the predicted relaxation to variability in the model parameters was assessed. The predicted residual stresses were validated using measurements made with the deep hole and incremental deep hole drilling techniques and the contour method.

## 1 Introduction

Weld residual stresses can have significant, undesirable effects on the structural integrity of high-value, safety critical engineering plant [1]. Estimating the levels and spatial distribution of weld residual stress is often not straightforward. Structural integrity assessment procedures such as R6 [2], BS7910 [3] and API 579 [4] include

both compendia of weld residual stress distributions for common weld geometries and, in the case of R6, advice on other estimation methods. R6 recognises three “levels” of weld residual stress, of decreasing conservatism and increasing complexity: “Level 1” consists of a uniform stress equal to the material yield strength across the cross-section of interest; “Level 2” stresses are upper bounds for common weldment geometries; while “Level 3” stresses are derived from a combination of finite element modelling and residual stress measurements on weldment mock-ups.

The level 2 residual stress profiles in R6 are based upon upper bounds to measured residual stresses, developed and updated by review of published data. These have the undesirable feature of tending towards a uniform through-wall distribution of stress equal to the material yield strength, as more published data are incorporated. This behaviour is driven by scatter and errors in measurements derived from a large number of sources of variable quality (see the discussion in [5]).

The use of finite element techniques to predict weld residual stresses is relatively mature [6, 7], and R6 includes detailed advice on finite element prediction of weld residual stresses in austenitic stainless steels, and their validation using measured data [8, 9]. The problem of scatter in residual stress measurements can be sidestepped using modelling, which allows extensive parametric studies covering a wide range of component geometries and weld types, all at much lower cost than manufacturing, characterising, and measuring residual stresses in large numbers of representative weldments. Modelling also produces full-field descriptions of residual stresses, in contrast to the point, line, or plane-based data obtained from measurements [10, 11]. Dong and co-workers have performed an extensive series of such studies over a number of years [12-16]. These have identified the key geometric and weld process variables influencing the form of pipe girth weld residual stress fields. A combination of finite element simulation and analytical shell theory have then been used to develop parametric formulations for both the through-wall distribution of weld residual stress at the weld centreline, and its axial die-away behaviour [16].

The residual stress profiles developed in [13-16] are based wholly upon modelling. Measured residual stresses are used only for validation of the modelling approach using published data for selected weldment mock-ups (for example the mock-up reported in [17, 18] and a selection of the mock-ups reported in [19]). Bouchard [19] has developed an analytical formulation for through-thickness residual stress profiles

in conventional austenitic stainless steel pipe butt welds, also intended to be used for defect tolerance assessment. This formulation is based on a combination of mock-up residual stress measurements on nine large-scale mock-ups, and finite element simulations originally reported by Bradford [20], using data available up to approximately 2001 (for example, see [21]).

Uncertainties in finite element predictions remain a serious concern. The guidelines for finite element prediction of weld residual stresses incorporated into the R6 procedure [8, 9] impose strict validation requirements on those predictions, driven in part by early experience with round-robin weld residual stress prediction activities [22-24]. The level of validation required depends on the structural integrity significance of weld residual stresses in the weldment being considered, but wholly unvalidated finite element predictions may not be used in structural integrity assessments made using R6.

Validation of finite element weld residual stress predictions requires representative, closely characterized mock-ups with reliable and repeatable residual stress measurements, preferably made using diverse methods with different characteristic errors (for example, diffraction-based and strain relief methods). The NeT collaboration has produced several high-quality benchmarks with large bodies of residual stress measurements. These include:

- NeT TG1: a single finite length gas tungsten arc (GTAW) weld bead made with AISI 316L welding wire, laid on an AISI 316L austenitic steel plate [25-28].
- Net TG4: a three-pass GTAW weld made with AISI 316L welding wire, laid in a finite length slot in an AISI 316L(N) austenitic steel plate [29-32].
- NeT TG5: a beam specimen in SA508 Gr 3 Cl 1 low alloy pressure vessel steel with a single autogenous GTAW weld pass along one edge [33, 34].
- NeT TG6: a three-pass GTAW weld made with Alloy 82 welding wire, laid in a finite length slot in an alloy 600 nickel alloy plate [35].

NeT adopt the approach of characterizing their benchmarks to a very high level. Multiple residual stress measurements using diverse techniques are accompanied by detailed characterization of the welding process and its associated thermal transients, and extensive materials property testing. This approach ensures both that finite

element simulations made to predict the weld residual stresses have the minimum possible uncertainty in their input data, and that the validation data for the simulation end products, residual stresses and distortions, are reliable and representative.

The work of NeT has confirmed that mixed isotropic-kinematic hardening models lead to the most accurate predictions of weld residual stresses in AISI 316L and AISI 316L(N) austenitic steel welds with limited numbers of weld passes [27, 29, 31].

The NeT benchmarks are all small weldments with limited numbers of weld passes, so cannot act as fully representative validation examples for multi-pass welds in large engineering structures. These require larger scale mock-ups. Such components tend to be rare, because of the costs involved in their manufacture, the difficulties encountered in making reliable, diverse and repeatable residual stress measurements in large components, and the burden of detailed material property characterization required for reliable benchmarking of simulations. Recent examples are the programmes run independently by British Energy (now EDF Energy) in the UK [36-40] and by EPRI/NRC in the USA [41, 42], both examining residual stresses in PWR primary circuit dissimilar metal welds. These programmes delivered mixed results: while it is possible to obtain predicted residual stresses that agree well with measured stresses [39], considerable scatter in predicted stresses can occur [41, 42], and it can be extremely difficult in these complex weldments to identify and account for all the sources of analysis variation. Mixed hardening models produced the most accurate predictions of residual stress in [40] (although strictly, of the three DMW constituents only AISI 316L and Alloy 82/182 were assumed to follow a mixed hardening rule: SA508 Gr 3 low alloy steel was assumed to harden kinematically, a decision underwritten by work on the NeT TG5 benchmark).

Plain girth welds in austenitic steels are usually considered to be a more tractable problem than dissimilar metal welds, witness the extensive work of Dong and co-workers [12-16, 22, 43]. However, validation remains a live issue. The profiles developed by Bouchard are supported by residual stress measurements made on nine separate weldments [19]. These measurements were limited to techniques available at the time, and in some cases diverse measurements were either not feasible, or they produced divergent results. The simulations underlying [19] also, of course, used techniques and knowledge available at the time. The residual stress measurement techniques available for thick section welds have improved significantly in recent

years. The conventional deep hole drilling technique, which was applied to the majority of mock-ups considered by Bouchard, is susceptible to plasticity induced errors when the residual stresses approach yield, and the incremental deep hole drilling method has been developed to minimize such errors [44]. Similarly, the contour method [11] has undergone continuous development, and can now be applied to large-scale structures such as dissimilar metal welded nozzles and pipe butt welds.

A number of thick-walled austenitic steel pipe girth weld mock-ups have been manufactured by British Energy (now EDF Energy) for an internal research programme, and then utilized by the STYLE Framework 7 project [45]. The mock-ups were fabricated under carefully controlled conditions, and residual stress measurements made using diverse techniques in both the as-welded state, and after thermal ageing at high temperature. An extensive programme of mechanical property evaluation was performed in parallel with mock-up manufacture and characterisation, on both parent material and the matching manual metal arc (MMA) weld metal [46].

These mock-ups offer an opportunity to assess the state of the art in weld residual stress prediction in a large-scale, plant relevant geometry. This assessment can cover both start-of-life residual stresses and the prediction of creep relaxation in high-temperature service. This paper forms the second part of this assessment. Part 1 [47] describes the manufacture, characterisation, and residual stress measurements performed on the pipe girth weld mock-ups, reports the detailed mechanical testing performed to establish the cyclic hardening behaviour of both parent material and manual-metal arc weld metal, and describes the approaches used to fit the parameters for the mixed isotropic-kinematic hardening models used to describe material behaviour during welding. Part 2, this paper, describes the finite element simulation campaign, which was performed in two stages. Stage 1 investigated the impact of the complex manufacturing history on the predicted residual stress state, while Stage 2 examined the impact of the material evolutionary hardening behaviour and creep deformation behaviour on the residual stress states after completion of manufacture, and after long term high temperature exposure. The phase 2 modelling laid particular emphasis on examining the evolutionary hardening behaviour of weld metal. This is less straightforward to characterise and model than parent material. The source and heat treatment state of the weld metal to be tested must be chosen carefully (specimens may be extracted from single pass, multi-pass pad, or multi-pass

weldment, and may be tested in the as-welded, solution treated, or intermediate annealed condition [31, 47]). It is also necessary to interpret the results of isothermal cyclic tests carefully, to ensure that both the start point (molten and strain free), and the end point (yield properties measured in multi-pass weld metal) of the modelled weld metal are correct.

## 2 Description of mock-ups

A welded pipe assembly was fabricated from Esshete 1250, an austenitic stainless steel with added vanadium and niobium to increase its high-temperature strength. The layout of the completed welded pipe assembly, consisting of 4 full-length (200 mm long) and 2 half-length (100 mm long) pipes, and five welds, is shown in Figure 1. The outer diameter was 180mm and wall thickness 35mm, giving  $R_m/t=2.1$ . After completion of welding the assembly was cut into five individual mock-ups, each of length 200mm. Full details of the fabrication process are given in Part 1 of this study [47].

## 3 Weld and materials characterisation

The extensive programme of residual stress measurement and mechanical property testing is described in Part 1 of this study.

## 4 Weld residual stress simulation

The girth weld mock-ups have a complex manufacturing history, all elements of which have the potential to affect the as-welded residual stresses. The simulation campaign was therefore conducted in two phases.

- In Phase 1, already partially reported in [48], the entire manufacturing history of the pipe assembly was modelled, comprising quenching, machining, welding, cutting of the assembly into individual weldments, and machining of the bore protrusion.
- In phase 2, the modelling was simplified to consider only welding and subsequent thermal soak of a single girth weld, neglecting the manufacturing history. The mixed hardening models calibrated in Part 1 of this study were applied in an extensive sensitivity study to assess the accuracy of the predicted

as-welded residual stresses, and the stresses after long term exposure to high temperature were predicted using creep deformation models currently used in the nuclear industry.

#### 4.1 Simulation philosophy and mesh design

The analyses comprised uncoupled heat transfer (thermal) analyses and subsequent stress and creep (mechanical) analyses, using ABAQUS 6.11 and later versions [49], adopting an axi-symmetric idealisation and small displacement assumptions. The welding heat sources were calibrated using a specialist fitting tool, FEAT-WMT [50].

##### 4.1.1 Phase 1: full manufacturing history

The Phase 1 analysis campaign followed the full manufacturing history of the pipe assembly, and was performed in five stages, see Figure 2, using a series of meshes optimised for the manufacturing stage(s) considered. The results were transferred from one stage of the analysis to the next using the “Map Solution” keyword in ABAQUS.

###### *Stage 1: Quenching.*

The water quench was modelled by applying a single heat transfer coefficient of  $16742 \text{ W.m}^{-2}.\text{C}^{-1}$  with a sink temperature of  $100^\circ\text{C}$  to the entire surface of the blanks, which were set at an initial temperature of  $1080^\circ\text{C}$  (Figure 2a). Note that although the mesh of each cylinder appears to be in contact with the next, there is no physical connection and the thermal transient is applied to all surfaces of each cylinder. At temperatures below  $100^\circ\text{C}$ , when boiling has ceased, a heat transfer coefficient of  $0.0005 \text{ W.m}^{-2}.\text{C}^{-1}$  was applied to the entire surface to slowly cool the pipe sections to  $20^\circ\text{C}$ .

This stage of manufacturing was modelled as sequential heat transfer and mechanical analyses, with the nodal temperature history from the heat transfer analysis applied as a thermal load in the mechanical analysis.

###### *Stage 2: machining.*

The solution from the mechanical quenching analysis was mapped onto the new mesh shown in Figure 2b, designed to simulate final pipe machining and insertion of the weld preparations. The manufacturing sequence of the welds allowed only Welds 1, 2

and 5 to be modelled directly. Welds 3 and 4 are identical to Welds 1 and 2, and were judged not to affect the residual stress fields in the other welds.

The J-grooves for the weld preparation have 15° sidewall angles, and the weld procedure allows a root gap of up to 1mm. Considerable axial shrinkage and tourniquet distortion occurs in pipe girth welds, meaning that the effective cross-section of the weld, and therefore both the amount of weld filler metal used and the cross-sectional areas of individual beads, are less than might be inferred from the original weld groove geometry. This effect was accounted for by eliminating the root gap, and by reducing the sidewall angle to 13°.

A mechanical analysis was performed to remove the machined material and allow the quench stresses and strains to re-distribute.

### *Stage 3: welding.*

The solution from the machining analysis was again mapped onto a new mesh designed to model the welding process for Welds 1, 2 and 5, see Figure 2c. The root, hot and fill passes were all modelled as simple trapezoids (see the inserts in Figure 2c). The root passes were modelled with a protrusion on the inner bore to reflect the as-welded configuration. The bead layouts for the hot and fill passes (passes 2-22) were obtained from the pass sequence maps kept as part of the welding records. The weld preparation cross sectional area was apportioned between passes in accordance with their relative heat inputs, since the bead cross-sectional area is known to be proportional to the energy input per unit length [51]. The capping pass geometries were based upon surface profile measurements made on the completed welds, simplified to trapezoids. Welds 1 and 2 have 3 capping passes, making a total of 25 passes, and Weld 5 has 2 higher heat input capping passes, making a total of 24 passes.

Welding was modelled as sequential heat transfer and mechanical analyses, and more complete details are given in Sections 4.3 and 4.4.

### *Stage 4: root protrusion removal and cutting into individual weldments.*

In this stage of the analysis, the root protrusion was removed, followed by cutting of the entire pipe assembly into the final test specimens, each having a girth weld at mid-length.

### *Stage 5: thermal ageing.*

Thermal ageing was modelled using the same mesh as the welding stage of the analysis. The temperature was raised to 650°C, and creep relaxation was modelled using user-defined creep laws for Esshete 1250 via a \*VISCO step in ABAQUS.

#### 4.1.2 Phase 2: Sensitivity to material hardening behaviour

The Phase 1 results discussed below showed that residual stresses on the weld centreline are essentially unaffected by details of the prior manufacturing history. The modelling approach was thus greatly simplified for the Phase 2 studies. A single, more refined axi-symmetric mesh was constructed containing Weld 5 alone (the central two-capping pass weld), as shown in Figure 3. This had a longer plain pipe section than the final completed pipes, which provides restraint intermediate between the original manufactured pipe assembly and the final completed test specimen CY7/CY6 after cutting.

Welding was modelled as sequential heat transfer and mechanical analyses, and thermal ageing was modelled on the same mesh, using the same approach as the Phase 1 analyses.

## 4.2 Material properties

### *Thermo-physical and physical properties*

The thermo-physical and physical properties of Esshete 1250 are given in Table 1. Esshete 1250 weld metal shows elastic anisotropy. Its effects on residual stress development and creep deformation were simply accounted for by reducing Young's Modulus by approximately 20%. This approach was adopted using insights gained from historical simulations made using elastically orthotropic material properties.

### *Mechanical properties*

The mechanical properties of Esshete 1250 parent and weld metal are presented in Part 1 of this study.

Every simulation except one used the Lemaitre-Chaboche mixed isotropic-kinematic hardening model [52], with the model parameters derived and reported in Part 1 of this study. As implemented in ABAQUS [49], the isotropic and non-linear kinematic parts of the model are described separately. The kinematic hardening component

describes translation of the yield surface in stress space via the backstress tensor  $\boldsymbol{\alpha}$ . The pressure-independent yield surface  $f$  is defined by the function:

$$f(\boldsymbol{\sigma} - \boldsymbol{\alpha}) = \sigma^0 \quad (1)$$

where  $\boldsymbol{\sigma}$  is the stress tensor,  $\sigma^0$  is the radius of the yield surface and  $f(\boldsymbol{\sigma} - \boldsymbol{\alpha})$  is the equivalent von Mises stress, defined by:

$$f(\boldsymbol{\sigma} - \boldsymbol{\alpha}) = \sqrt{\frac{3}{2}(\mathbf{S} - \boldsymbol{\alpha}^{\text{dev}}) : (\mathbf{S} - \boldsymbol{\alpha}^{\text{dev}})} \quad (2)$$

here  $\boldsymbol{\alpha}^{\text{dev}}$  is the deviatoric part of the back stress tensor, and  $\mathbf{S}$  is the deviatoric stress tensor, defined as  $\mathbf{S} = \boldsymbol{\sigma} + p\mathbf{I}$ , where  $p$  is the equivalent pressure stress, and  $\mathbf{I}$  is the identity tensor.

The kinematic hardening component is defined as an additive combination of a purely kinematic term (the linear Ziegler hardening law) and a relaxation term (the recall term), which introduces nonlinearity. When temperature and field variable dependencies are omitted, the kinematic hardening law is:

$$\dot{\boldsymbol{\alpha}}_k = C_k \frac{1}{\sigma^0} (\boldsymbol{\sigma} - \boldsymbol{\alpha}) \dot{\bar{\boldsymbol{\varepsilon}}}^{\text{pl}} - \gamma_k \boldsymbol{\alpha}_k \dot{\bar{\boldsymbol{\varepsilon}}}^{\text{pl}} \quad (3)$$

And

$$\boldsymbol{\alpha} = \sum_{k=1}^n \boldsymbol{\alpha}_k \quad (4)$$

where  $C_i$  and  $\gamma_i$  are material parameters that must be calibrated from monotonic or cyclic test data.  $C_i$  is the initial kinematic hardening modulus, and  $\gamma_i$  determines the rate at which the kinematic hardening modulus decreases with increasing plastic deformation.  $\boldsymbol{\sigma}$  is the stress tensor,  $\sigma^0$ , is the equivalent stress defining the size of the yield surface, and  $\dot{\bar{\boldsymbol{\varepsilon}}}^{\text{pl}}$  is the equivalent plastic strain rate. As noted above, only the deviatoric part of  $\boldsymbol{\alpha}$  contributes to the material hardening behaviour. When  $C_i$  and  $\gamma_i$  are both zero, the model reduces to pure isotropic hardening.

The isotropic hardening component of the model defines the evolution of the yield surface size,  $\sigma^0$ , as a function of the equivalent plastic strain, or plastic path length,  $\bar{\boldsymbol{\varepsilon}}^{\text{pl}}$ .

$$\sigma^0 = \sigma|_0 + Q_{\text{inf}} \left(1 - e^{-b\bar{\epsilon}^{\text{pl}}}\right) \quad (5)$$

where  $\sigma|_0$  is the yield stress at zero plastic strain, and  $Q_{\text{inf}}$  and  $b$  are material parameters.  $Q_{\text{inf}}$  is the maximum change in the size of the yield surface, and  $b$  defines the rate at which the size of the yield surface changes as plastic straining develops.

The parent material parameter sets available for this study are listed in Table 2. The Phase 1 studies made use of parent models 1 and 4, while the Phase 2 studies made use of parent models 2 and 4.

The weld metal parameter sets available for this study are listed in Table 3. The Phase 1 studies made use of weld metal models 1 and 5, while the phase 2 studies employed a much larger range: models 4-9.

The work of the NeT network has confirmed that mixed isotropic-kinematic hardening models lead to the most accurate predictions of weld residual stress in small-scale austenitic steel benchmarks such as NeT TG1 and NeT TG4. Given this knowledge, only limited analyses were performed using simpler isotropic and kinematic hardening models.

A single Phase 2 analysis was performed using an isotropic hardening rule. The mechanical properties for this analysis were defined as piecewise-linear stress-strain curves, which were fitted to the total stress predicted by monotonic loading of parent model 2 and weld model 5 respectively. Parent model 2 uses two back-stresses fitted to monotonic loading, with  $Q_{\text{inf}}$  matched to 2.5% TSR tests, and Weld model 6 also uses two back-stresses, but fitted to first re-loading from compression of 1.5% TSR tests on single-pass weld metal, with  $\sigma^0$  reduced to simulate as-deposited weld metal, and with  $Q_{\text{inf}}$  increased to saturate at the 0.2% proof stress of multi-pass weld metal. Both the isotropic models employed perfectly plastic cut-offs, set at 30% plastic strain for parent material and 10% plastic strain for weld metal. At room temperature these correspond to saturation at 487 MPa for parent material and 533 MPa for weld. These may be compared with cyclic saturation limits of ~470 MPa at 2.5% TSR for Parent model 2, and 551 MPa at 2.5% TSR for Weld model 6. The choice of saturation limit is important, because it limits the peak stresses that may be predicted in the analysis.

A single Phase 2 analysis was also performed using a kinematic hardening rule. The mechanical properties for this analysis were defined by setting  $Q_{\text{inf}}$  to zero for parent

model 2 and weld model 6 respectively. Kinematic hardening models correctly incorporate the Bauschinger effect, which is important in cyclic loading processes such as welding. The lack of any cyclic isotropic hardening means that kinematic models normally predict welding stress distributions with lower amplitudes than alternative formulations [22, 37-39, 41, 53], and where validation is available (eg [29, 38, 54]) their use leads to under-prediction of the measured stress amplitudes.

#### *High temperature behaviour during welding*

It is common practice to approximate high temperature recovery and re-crystallisation processes using a simple “annealing” rule. This procedure was followed here. The ABAQUS \*ANNEAL TEMPERATURE functionality was used to eliminate the isotropic hardening component above a fixed temperature (either 1100°C or 1300°C depending on the analysis), by setting the equivalent plastic strain to zero. This has the effect of re-setting the radius of the yield surface to its initial value, see Equation (4). The kinematic back-stress was re-set to zero at and above 1000 °C by zeroing the hardening moduli in Equation (3).

#### *Creep deformation behaviour*

The RCC-MR design code [10] defines a creep law which separates the primary and secondary creep regimes:

$$\varepsilon^c = \begin{cases} C_1 t^{C_2} \sigma^{n_1}, & t \leq t_{fp} \\ C_1 t_p^{C_2} \sigma^{n_1} + C \sigma^n (t - t_{fp}), & t > t_{fp} \end{cases} \quad (7)$$

where  $C_1$ ,  $C_2$ ,  $n_1$ ,  $n_2$  and  $C$  are material constants defined in the RCC-MR design code and  $t$  is time (in h). The primary creep strain has a power-law relationship with stress and time. The secondary creep strain is in the form of (7) in addition to a maximum primary creep strain which is evaluated at the transition time,  $t_{fp}$ . The RCC-MR code states these expressions are valid up to 1% creep strain. The primary creep formula applies for temperatures between 425°C and 700°C and the secondary creep formula for temperatures between 480°C and 700°C. The constants for the RCC-MR model for Esshete 1250 weld metal are shown in Table 4.

Creep strain rates may be defined for the material models with each of the hardening laws by defining  $\dot{\varepsilon}^c$  as a function of time or strain. Differentiating the RCC-MR creep model for the primary regime with respect to time gives:

$$\dot{\varepsilon}^c = C_1 C_2 t^{C_2-1} \sigma^{n1} \quad (7)$$

Substituting Eq.(7) into Eq. (6) gives the strain hardening formulation

$$\dot{\varepsilon}^c = (C_1 \sigma^{n1})^{\frac{1}{C_2}} C_2 \varepsilon_c^{\frac{C_2-1}{C_2}} \quad (8)$$

The creep deformation behaviour was embodied in an ABAQUS user-defined subroutine [55]. Although this has the capacity to apply different creep deformation behaviour to different materials, it was assumed that the weld metal behaviour applied to the entire pipe. This was judged a reasonable approach, as stress relaxation behaviour would be dominated by the very high initial von Mises residual stresses in weld metal.

The coefficients for the RCC-MR law presented in Table 4 and identified as “baseline” had been fitted to creep deformation test data over a range of temperatures. The resulting parameters are known to under-predict creep deformation rates at temperatures approaching 650°C, since they are optimised for the lower temperatures at which Essete 1250 operates in the UK’s fleet of advanced gas cooled reactors. A series of sensitivity studies were performed to assess which parameters in the model most strongly affected the predicted stress relaxation in the pipe girth weld, and to optimise their values. It was found that only  $n$  and  $n1$  had any significant effect on the predicted stress relaxation. The parameter set identified as “optimised” were then derived. It can be seen that this was achieved by increasing  $n1$  from 8.9395 to 9.9395.

### 4.3 Thermal modelling

Experience with the NeT benchmarks [25, 27, 30, 32, 56, 57] has shown that the use of a specialised weld heat source modelling tool leads to the most reliable and accurate thermal analyses of welding processes. The simulations reported here used FEAT-WMT, a dedicated heat source modelling tool [50]. FEAT-WMT imports an ABAQUS mesh (2D, axi-symmetric, or 3D), and uses it to construct a 3D steady state moving mesh model of the weld concerned. This approximates steady-state conditions far from the start or stop end of a weld bead. FEAT-WMT then predicts the fusion boundary profile and transient temperature history close to the weld, offering the ability to compare these against measured profiles and thermocouple data. The tool contains a number of weld heat source models, and it is capable of superposing multiple heat sources for a single pass, and of dealing with complex torch

paths. Once an optimised thermal solution is obtained, FEAT-WMT offers an interface to ABAQUS via the DFLUX user subroutine. This uses volumetric heat flux data output as a series of time-slice files. The optimised heat source can be output as a 2D or axi-symmetric approximation, a 3D simultaneous bead deposition (aka “block dumped”) approximation, or as a full 3D moving heat source.

2D, axi-symmetric, and 3D “block-dumped” approximations assume that heat transfer in the direction of torch travel is not significant. This is the case if the weld Peclet number,  $P_e$ , is in excess of unity, where

$$P_e = \rho C_p v L_w / k$$

and where  $v$  is the linear torch speed,  $L_w$  is a characteristic length, taken to be the diameter of the heat source representing the torch in the welding direction, and  $\rho$ ,  $C_p$  and  $k$  are the density, specific heat and the thermal conductivity respectively of the material. Conventionally [2, 51] the properties of the parent material at 800°C are used to calculate this quantity. A typical Peclet number for the welds considered here is 4.6, for the capping passes, so an axi-symmetric heat source idealization will be adequate for the thermal analyses.

The process of generating an equivalent 2D heat source is fully automated within FEAT-WMT, ensuring that the correct heat input is applied to the model, and avoiding potential errors involved in writing a bespoke heat source solution for each individual FE mesh, and converting between the optimized 3D moving heat source and whatever 2D equivalent is used.

The simulations reported here used a simple Gaussian ellipsoidal heat source, defined by:

$$q = \frac{Q}{V_a} \exp\left(-\left(\left(\frac{x}{r_l}\right)^2 + \left(\frac{y}{r_v}\right)^2 + \left(\frac{z}{r_a}\right)^2\right)\right) \quad (5)$$

where

$$Q = \eta VI \quad (6)$$

In Equation (5)  $q$  is the power per unit volume,  $Q$  is total power deposited,  $(x,y,z)$  is the geometric centre of the distribution (by default at the geometric centroid of the weld bead as defined in the FE mesh), and  $r_l, r_v, r_a$  are the radii of the distribution in the lateral, vertical and axial directions, see Figure 4.

In Equation (6)  $\eta$  is the welding efficiency,  $V$  the arc voltage, and  $I$  the welding current.

The quantity  $V_a$  is not a user-specified parameter in FEAT-WMT, but is chosen automatically by the code on a particular mesh so that the total power input to the work is  $Q$ . It ensures that those parts of the heat source that are not within the currently active mesh are not lost. This is a common source of error in individually coded finite element heat source models [30].

In addition to the basic source parameters above, FEAT-WMT offers options to offset the centre of the source in the weld transverse plane, to change its angle, and to impose source weaving on arbitrary paths in the weld transverse plane.

Fitting a heat source with a number of parameters must follow a carefully defined procedure to avoid physically unreasonable solutions. When both weld thermocouple data and fusion boundary profiles are available then the procedures developed and validated within NeT may be used [27, 30], namely to first fit the global heat source intensity in Equation (6) by matching the temperature rises recorded at thermocouples far enough from the heat source that they are insensitive to its shape (effectively calibrating  $\eta$ ), and then to fit the heat source “shape” (radii, offsets, angle and source weaving) to match the fusion boundary profile revealed by weld transverse macrographs.

In many cases, lack of data prevents this ideal approach being followed. The welds being modelled here have no transient thermocouple data available, and the weld metallography is limited to completed welds, meaning that individual transverse weld bead profiles are known only for the final capping passes, although the total melted envelope is known. The global weld parameters,  $V$ ,  $I$ , and torch speed  $v$  are known, but  $\eta$  cannot be calibrated directly from measured temperature rises.

The lack of measured thermocouple data is judged unlikely to lead to significant errors in the final predicted residual stresses. The analytical through-wall residual stress profiles developed by Bouchard [19] for austenitic steel pipe girth welds are a

function of both weld geometry and heat input. Thick-walled pipes of the geometry considered in this study exhibit little sensitivity to credible variations in heat input,  $Q$ , when Bouchard's formulation is applied to estimate the through-wall axial residual stress profile.

The R6 weld modelling guidelines [2, 9] make a series of recommendations for heat source fitting procedures in the absence of thermocouple and fusion boundary profile data. These vary with the available data, and they were followed in this analysis.

The strategy adopted made use of the following knowledge:

1. The relationship between the cross-sectional area of weld filler metal introduced per pass and the electrical heat input per unit length  $VI/v$  is known for MMA welds in austenitic steels, at  $A_{bead}=15VI/v$ , see Figure 5.
2. The total fusion boundary envelope of the completed weld is known from transverse metallography, which reveals significant axial contraction from the nominal weld preparation.
3. The total melted area per bead (filler plus fused parent or previously deposited filler) is known to be about twice the area of filler introduced in that pass [51].

Inspection of the weld metallography led to the decision to model the weld preparation with no root gap and a sidewall angle reduced to  $13^\circ$  from  $15^\circ$ . The total area within the weld groove was then calculated and compared with the area of deposited weld metal inferred from the published correlation of Figure 5 (the data for pipe CY7/CY6 and weld 5 are presented in Table 5). The two calculated areas agreed closely, validating the decision to reduce the groove area. The area occupied by the hot and fill passes (2 to 22 in CY7/CY6) was then divided between passes in proportion to their heat inputs, and the capping pass areas were calculated from their heat inputs, see Table 5.

Heat source parameter fitting was achieved as follows:

1. The three source radii were set equal to each other (a spherical source)
2. No offsets or angular changes were used, so all sources were centred at the bead centroid.
3. The source radii for the MMA passes were set equal to the electrode diameter used, to reflect the fact that extent of the arc will increase with electrode size.

The source radii for the root and hot passes, made using TIG, were not fixed a priori, since it proved impossible to predict credible fusion boundary profiles without using them as a fitting parameter.

4. Sinusoidal lateral source weaving was allowed, in accordance with the weld procedure.
5. A target efficiency of between 75% and 85% was set, based upon extensive experience with modelling MMA processes.
6. The efficiency and source weave amplitude were then adjusted to ensure that the entire introduced weld bead melted, and that the total melted cross-sectional area for the pass was  $\sim 2x$  the introduced filler area. For passes 1 and 2, it also proved necessary to adjust the heat source radii to achieve sensible melted profiles in the unusually shaped beads (see Figure 3).

The final source parameters for pipe CY7/CY6, weld 5, are given in Table 5. The accumulated fusion boundary profile predicted using FEAT/WMT for the same weld is compared with the weld transverse macrograph in Figure 6. It can be seen that the use of gaussian ellipsoidal heat sources results in realistic individual pass fusion boundary profiles, despite the use of trapezoidal weld beads in the FE mesh. It is also evident that the predicted weld envelope appears to be slightly wider than that observed in the pipe, especially at the weld root, although the weld cap width is correct. Since the capping passes tend to dominate the final residual stress profile, this should not be a concern.

#### 4.4 Mechanical modelling

The overall mechanical analysis sequence adopted for both Phase 1 and Phase 2 studies has been described above. The major variables examined in the extensive matrix of analyses were:

1. The impact of manufacturing history on the final as-welded residual stress state
2. The impact of changes to the structural boundary conditions during welding
3. The impact of changes in the mechanical properties of both parent material and weld metal.

Manufacturing history and boundary conditions were investigated as part of the Phase 1 study. Mechanical property changes were examined primarily within the Phase 2 study.

The impact of changes to the thermal solution was not investigated. The only significant unknown in the thermal solution is the welding efficiency. Multi-pass girth welds in thick-walled pipes are believed to be relatively insensitive to details of the thermal solution (for example, see [37, 38]). The extensive simulation campaign for the NeT TG4 benchmark has also shown little sensitivity to changes in the welding efficiency, in a small specimen with only three weld passes where its effects might be expected to be more marked [29, 30].

#### 4.4.1 Phase 1 analyses

The full sequence of analyses to simulate the manufacturing history has already been described. The effect of starting the analysis after quenching was complete, with stress-free pipe sections, was also examined.

The phase 1 studies employed two material property combinations, the “historical” single-back-stress parent model 1 and weld model 1, and the models identified as parent model 4 and weld model 5, see Table 2 and Table 3. Only results obtained using the historical models 1 are presented here.

It is conventional in axi-symmetric modelling of pipe girth welds to allow free axial expansion and contraction during welding if the welded assembly is not restrained. However, this approach neglects the restraint against axial expansion offered by material behind the weld pool of a moving weld torch that has already solidified, cooled, and gained strength. If this is ignored, especially in the early passes of a multi-pass weld where the entire ligament beneath the weld pool reaches high temperatures and softens, then the total axial contraction is significantly under-predicted (for example, see [40]). Bendeich et al [40] have developed a system of restraint whereby axial expansion is prevented, but contraction can take place freely, and applied this to a large-scale nozzle dissimilar metal weld mock-up. The application of axial restraint leads to accurate predictions of axial contraction, and to improvements in the accuracy of the predicted residual stresses. This axial restraint system was thus applied in a sensitivity study. Although no measurements of weld

contraction exist to validate the simulations, the impact of improved axial restraint on predicted residual stresses is of considerable interest in its own right.

#### 4.4.2 Phase 2 analyses.

The complete matrix of material property combinations examined in the phase 2 analyses is given in Table 6.

### 4.5 Modelling of thermal soak testing

After completion of welding and root removal, the temperature of the model was raised to 650°C, followed by steady state creep relaxation for 10,000 hr.

## 5 Results and discussion

### 5.1 As-welded residual stresses

The general development of residual stresses in the pipe sections is shown in Figure 7. The quenching process develops significant stresses, which are compressive near the pipe surfaces, and tensile near mid-thickness (Figure 7a). The welding process generates large stresses in the vicinity of the welds. These have the distribution expected for a thick-walled pipe butt weld. They appear to be unaffected by the prior quench stress/strain field, but quench stresses remain visible in those parts of the parent pipe that are more than one wall thickness from the welds (Figure 7c). Cutting into individual pipe sections and root machining have no visible effect on stresses near the welds, but do further relax quench stresses near the pipe ends. The remaining tensile quench stresses visible in Figure 7d are also present in the contour method measurements reported in Part 1 of this study [47]. The impact of capping pass layout is clearly visible: the region of peak hoop and high axial stresses beneath the outer surface always develops under the final pass deposited.

The weld residual stress fields are presented in more detail in Figure 8, for a representative Phase 2 analysis with no prior manufacturing history. It is evident that the stress field remote from the weld shows some differences with the “full history” analysis plotted in Figure 7.

The through-wall distribution of residual stress on the weld centreline is of most interest. It passes through the peak stress regions of all three welds (with the slight caveat that the absolute peak stresses in weld 5 are slightly offset, beneath the final

pass), samples all the major features of the weld residual stress field and diverse residual stress measurements are available only on this line (see Part 1 ). The focus of this study is on the most representative evolutionary hardening model to use for weld metal, so concentrating on the weld centreline is appropriate.

The contour plots suggest limited effects of history on the final residual stress field within the welds themselves, and this may be confirmed by examining line plots. Figure 9 plots the final residual stresses predicted for Weld 5 for two Phase 1 analyses using the historical weld and parent materials 1: one incorporates the full manufacturing history, while the second omits the quenching and machining steps and starts with pipe girth welding. Both analyses show very similar through wall stress distributions:

- Hoop stresses rise from  $\sim 380$  MPa at the outer surface of the weld cap, peak at  $\sim 580$  MPa about 5 mm beneath the outer surface, then fall into compression. The minimum stress is  $\sim -430$  MPa, reached at about 11mm from the inner surface, and the stress then rises to  $\sim -320$  MPa at the inner surface.
- Axial stresses show a sinusoidal distribution, rising from  $\sim -100$  MPa at the outer surface of the weld cap, peaking at  $\sim 230$  MPa about 8 mm beneath the outer surface, and then falling into compression. The minimum stress is  $\sim -290$  MPa, reached at about 13mm from the inner surface, and the stress then rises to close to zero at the inner surface.

Inclusion or omission of quenching and machining perturbs the final predicted hoop stresses at the centre of the weld by less than 20 MPa. It has even smaller effects on the axial stresses. Other operations in the manufacturing sequence have effects on the final stress state that are comparable or even less significant, see [48]. In particular, the manufacture of adjacent welds, at a spacing of 200mm (approx. 6t) has negligible effects, as does root machining.

The cap geometry does have visible effects on stresses near to the outer wall. Figure 10 plots the final residual stresses predicted for Welds 1, 2 and 5 for a Phase 1 analysis using the historical weld and parent materials 1, that followed the entire manufacturing history. The capping pass location only affects the tensile stress region near the outer surface: if the capping pass is on the weld centreline (welds 1 and 2) rather than offset (weld 5), then the peak hoop stresses are displaced deeper by about

3mm, without any significant difference in peak stress, while the tensile peak in axial stress rises by  $\sim 40$  MPa ( $\sim 20\%$ ). The residual stress measurements were made both on a two-capping pass weld (contour method on CY7/CY6) and a three-capping-pass weld (iDHD on CY5/CY9), so these differences need to be considered in interpretation of the data.

The effect of axial restraint is shown in Figure 11. This plots stresses for Weld 5, using the historical parent material and weld metal 1 model parameters. Imposing more realistic axial restraint conditions has visible effects, especially on axial stresses. The peak tensile axial stress rises by  $\sim 50$  MPa (about 22%), and the peak compressive axial stress falls by a similar amount. If the stress distribution was decomposed into membrane, through-wall bending and higher order components then the through-wall bending stress would be observed to increase, while the membrane stress would remain at zero and the higher order components would change little. The tensile hoop stresses near the outer wall do not change, while stresses near the inner wall fall slightly, by  $\sim 40$  MPa ( $\sim 10\%$ ). This is qualitatively identical behaviour to that predicted by Bendeich et al in a dissimilar metal weld [40].

Figure 11 also plots the as-welded residual stresses measured on the weld centreline using iDHD and the contour method. The contour method axial stress measurements are the average of all the through-wall profiles measured (see Figure 8 of Part 1 [47]). These are not presented in order to make detailed numerical comparisons between simulation and measurement, since the simulations make use of only one set of material model parameters. Rather, they allow us to compare the changes in predicted stress due to more “representative” axial restraint with the scatter in measurements. It is evident that the predicted changes in axial stress are similar in magnitude to the differences between iDHD and contour method mean profile, and lower than the spread observed in the contour method data (see Figure 8 of Part 1 [47]). The predicted hoop stresses only change near the inner wall, and here they move closer to the contour measurements, although too much should not be made of this observation. Thus, although it is probable that imposing axial restraint results in a more accurate prediction, the changes in predicted stress that it causes, with the chosen set of material model parameters, are within the variability of the measured stresses.

The phase 2 studies took advantage of the demonstrated insensitivity to manufacturing history and used a single-weld FE mesh to examine sensitivity to

material hardening behaviour. Neither prior history nor axial restraint were modelled. Extensive studies performed on the NeT TG1 single bead-on-plate and NeT TG4 three-pass slot weld benchmarks have shown that predicted residual stresses in these “simple” plate specimens are very sensitive to the assumed material hardening behaviour. Is this still true for a multi-pass pipe girth weld?

The effect of fundamental hardening model is shown in Figure 12 and Figure 13, for hoop and axial stress respectively, on the weld centreline, for the following material assumptions

- The isotropic hardening analysis, plotted in red, that makes use of piece-wise linear fits to the total stress predicted for monotonic loading of Parent model 2 and Weld model 6 respectively.
- A kinematic hardening analysis, plotted in yellow, using the same Chaboche model fits (Parent 2 and Weld 6), but with  $Q_{inf}$  set to zero to suppress cyclic hardening.
- Four mixed hardening analyses all using Parent model 2<sup>1</sup>, but using four different weld metal models.
  - Two, Weld models 5 and 7, made no adjustment to the value of  $Q_{inf}$  measured from tests, so the models did not harden to the yield strength of multi-pass weld at low temperatures. The two models differ in their handling of initial yield strength, with that of Model 7 being reduced to account for the work hardening already present in the single pass weld metal used for testing and parameter fitting. Results for these two models are plotted in blue.
  - Two, Weld models 4 and 6, had  $Q_{inf}$  increased to ensure that the models cyclically hardened to the yield strength of multi-pass weld metal at all temperatures. Again, the two models differ in their handling of initial yield strength, with that of Model 6 being reduced to account for the work

---

<sup>1</sup> Simulations performed on the NeT TG4 benchmark indicate that fitting the kinematic behaviour of parent material to the monotonic response is to be preferred for AISI 316L(N), and at the centreline of the Esshete girth welds analysed here changing between monotonic and cycle 2 fits (Parent models 2 and 4) has virtually no effect on the predicted stresses.

hardening already present in the single pass weld metal used for testing. Results for these two models are plotted in green.

Also plotted on Figure 12 and Figure 13 are the measured stresses at start of life. Changing the hardening models does not change the general form of the through-wall stress distributions: the hoop stresses are tensile near the outer wall and compressive near the inner wall, while the axial stresses show a sinusoidal distribution with tension beneath the outer surface and compression beneath the inner surface. The amplitude does change markedly, however:

- The lowest amplitude is predicted by the kinematic hardening analysis, with hoop stresses varying between +300 MPa and -50 MPa, and axial stresses between +120 MPa and -140 MPa
- The two mixed hardening analyses that make no adjustment to the cyclic saturation limit of Esshete weld metal predict higher stresses, with hoop stresses ranging from +450 MPa to -200 MPa, and axial stresses from +200 MPa to -240 MPa.
- If the cyclic saturation limit of the weld metal model is increased to achieve the yield strength of multi-pass weld metal, then the stress amplitudes rise further, with hoop stresses varying from +600 MPa to -430 MPa, and axial stresses from +250 MPa to -310 MPa
- As expected, the highest stress amplitudes are predicted by the isotropic hardening analysis, with hoop stresses varying from +600 MPa to -520 MPa, and axial stresses from +305 MPa to -445 MPa

The low stress amplitudes predicted using kinematic hardening are no surprise, given the significant cyclic hardening exhibited by Esshete 1250, and are consistent with previous modelling studies [22, 53, 54]. The assumed weld metal hardening limit has very visible effects on the stresses predicted using mixed hardening models, with larger stress amplitudes predicted if the hardening limit is adjusted to match the measured weld metal yield strength. And, as expected, assuming isotropic hardening leads to the highest stress amplitudes. It is noteworthy, however, that, especially in the hoop direction, the difference between isotropic hardening and mixed hardening with adjusted hardening limit is less than observed in simple one and three pass benchmarks such as NeT TG1 and TG4 [27, 29]. This suggests that the weld metal

model has saturated over much of the cross-section, as the saturation limits of the isotropic weld model and mixed hardening models 4 and 6 are intentionally similar. If the isotropic model had been based upon uniaxial tensile data with no cut-off at an appropriate saturation stress, its use would have led to much more significant over-prediction of stress amplitudes.

Comparison with the measurements suggests that the mixed hardening model analyses with increased weld metal saturation limits are the most accurate, as they sit near the bounds of the measured axial stresses (see Figure 8 of Part 1 [47]) and provide the best overall match with the measured hoop stresses, albeit with an apparent over-prediction of nearly 200 MPa for the peak tensile hoop stresses beneath the capping passes. It is possible that the peak hoop stresses are slightly under-measured. The iDHD method can under-measure due to plasticity effects. The contour method can produce similar effects due both to plasticity during the cutting process, and over-smoothing of the residual stress field during data analysis. It is also clearly possible that the apparent over-prediction is real.

Reductions made to the initial yield strength of the weld material model to account for the presence of work-hardening in the single-pass weld metal used for testing only affect stresses in the last deposited pass, at fractional distances through the wall of  $>0.85$ , see Figure 12.

A possible contributing factor to apparent over-prediction of stress is the cyclic hardening rate, controlled by the parameter  $b$ . Table 7 of Part 1 of this study shows that Essete weld metal cyclically hardens much faster near room temperature than in the range  $400^{\circ}\text{C}$ - $600^{\circ}\text{C}$ . The mechanics of the mixed hardening model mean that equivalent plastic strain accumulated at high temperatures will have a much stronger effect on prior hardening when the material cools to room temperature. This may be physically incorrect, so two sensitivity studies addressed this issue by reducing the hardening rate parameter at  $200^{\circ}\text{C}$  and below. The first, using weld model 8, reduced  $b$  from  $\sim 25$  to 10, and the second, using weld model 9, further reduced it to 5. Figure 14 and Figure 15 show the effect of reducing the weld metal model cyclic hardening rate, plotting the two additional simulations using weld models 8 and 9. Reducing the hardening rate reduces the amplitude of both the hoop and axial residual stress distributions. It appears to have broadly similar effects near both inner and outer

surfaces, so hardening rate alone does not appear able to account for the over-prediction of peak tensile hoop stresses.

Figure 16 plots the effect of weld model parameter sets on through-wall distributions of the equivalent plastic strain and the yield surface radius  $\sigma^o$ . With the exception of the last deposited pass at  $x/t > 0.85$ , where the strain is less than 2.5%, the general level of equivalent plastic strain is relatively uniform across the thickness, and very similar for all the weld models, albeit slightly higher for weld models with lower cyclic saturation limit,  $Q_{inf}$  or lower hardening rate,  $b$ , especially near the weld root. The short wavelength variations caused by deposition of successive weld beads are clearly visible. The weld models with high hardening rates are fully cyclically saturated over the entire thickness, except for the final pass. The two models with reduced hardening rates (models 8 and 9) are not fully saturated, so predict lower yield surface radii than the equivalent high hardening rate models (models 4 and 6), albeit with oscillations in  $\sigma^o$  that match the variation in equivalent plastic strain. Despite not having saturated, the predicted yield surface diameter remains relatively uniform over most of the thickness, a reflection of the distribution of plastic strain.

The yield surface diameter is not the only parameter affecting the position of the yield surface – the back-stress  $\alpha$  is also important. Figure 17 plots the effect of weld model parameter sets on through-wall distributions of both the hoop stress, and  $\alpha_{33}$  the hoop component of the back stress. There is no difference in  $\alpha_{33}$  at the location of peak tensile stress, indicating that the amount of isotropic hardening is controlling the peak stress, while the differences in  $\alpha_{33}$  at the peak compressive stress location are small, again suggesting that isotropic hardening is controlling the peak stress.

Some insight into the actual hardening distribution from top to bottom of the weld may be obtained by plotting the measured hardness variation. This is plotted on Figure 18, as lines with diamond markers. The hardness within the capping passes is low, rising rapidly at depths where the material moves from a single cooling cycle to 1.5 thermo-mechanical cycles. It then rises steadily with increasing depth. This contrasts with the cyclic hardening limits plotted in Figure 16, which exhibit similar behaviour within or just below the capping passes, but then show no further rise with increasing depth, in line with the predicted equivalent plastic strains.

One possible reason for this discrepancy is the effect of axi-symmetric boundary conditions on the through-wall plastic strain distribution. Imposing more realistic axial restraint increases the overall axial contraction during welding, and this is associated with an increase in equivalent plastic strain at the weld root. Figure 18 also plots, as open circles, the equivalent plastic strains for the phase 1 analyses, with and without axial restraint, already plotted in Figure 11. This shows a significant increase in plastic strain in the first 8mm from the weld root, and little or no effect elsewhere. The likely effect on the yield surface diameter  $\sigma^o$  is also plotted on Figure 18 for the four weld models. The yield strength at the root rises with improved axial restraint, but not by enough to match the through-wall slope in yield strength implied by the hardness measurements.

There clearly remain residual errors in the finite element predictions of as-welded residual stresses. They are probably due to a combination of slightly unrealistic structural boundary conditions associated with the axi-symmetric approximation, and inadequacies in the fitted Chaboche models. The latter may be due to the thermo-mechanical nature of the welding loads, but it should also be remembered that the developing microstructure of a multi-pass weld will differ from the single pass welds tested to develop the Chaboche model parameters.

## 5.2 Stresses after high temperature ageing

Measured and predicted stresses on a thorough wall line at the weld centreline are compared in Figure 19, hoop stress, and Figure 20, axial stress. The measured stresses are close to being biaxial with hoop stresses in the range  $\sim 140$  MPa to  $\sim -140$  MPa and axial stresses in the range  $\sim 110$  MPa to  $\sim -100$  MPa. The predicted hoop stresses agree closely with measurements if the optimised RCC-MR model parameters are used but are approximately 2x the measured stresses if the baseline parameters are used. Axial stresses show a broadly similar pattern, although the differences between the two sets of model parameters are less marked. The significance of under-predicting stress relaxation due to creep depends upon the degradation of failure mechanism being assessed. If fracture from a pre-existing defect is the concern, then it is conservative, or safe, to under-predict the amount of stress relaxation. Conversely, if the development of creep damage is the concern, as in reheat cracking,

then under-predicting stress relaxation is non-conservative, because it under-predicts the accumulated creep strain.

## 6 Conclusions

A detailed FE simulation has been performed, covering the entire manufacturing sequence of a welded assembly containing five pipe girth welds made in Esshete 1250, an austenitic stainless steel, extending to subsequent high temperature thermal ageing. The following conclusions have been drawn:

1. The quenching process after initial solution treatment of the pipe blanks produces significant residual stresses: however, weld-induced plasticity eliminates the quench stress field close to the welds. In pipe sections farther from the weld-affected area, the quenching stresses remain significant even after weld completion.
2. Residual stresses in completed girth welds in this geometry are affected very little by making subsequent welds at a separation of 200mm (5.7t), and both cutting of the entire weld assembly into test specimens each containing a mid-length girth weld, and removal of the root pass protrusion, each have little effect on the residual stress redistribution.
3. Imposing restraint on the axi-symmetric models to prevent axial expansion during welding leads to an increase in the amplitude of the through-wall distribution of axial stress, which agrees better with measured stresses.
4. As-welded residual stresses on the weld centreline may be predicted with good accuracy using mixed isotropic-kinematic hardening models.
5. Assuming pure kinematic hardening leads to predictions of as-welded residual stresses that show lower amplitudes than the measured stresses.
6. Assuming isotropic hardening leads to predictions of as-welded residual stresses that show higher amplitudes than the measured stresses, although the level of conservatism is mitigated by a) setting the model hardening limits close to the cyclic saturation limit of the materials, and b) the observation that levels of equivalent plastic strain in much of the multi-pass weld are high enough to lead to cyclic saturation of the weld mixed hardening models as well.
7. The most accurate predictions of stresses on the weld centreline are achieved if the weld metal model parameters are derived from tests on single pass weld metal,

with the initial yield strength reduced to account for work hardening already present in the tested material, and the cyclic hardening limit at low temperatures increased to ensure that the model hardens to the measured yield strength of multi-pass weld metal.

8. Stress relaxation due to thermal ageing at 650°C may be predicted with good accuracy using an RCC-MR type creep law, although the amount of relaxation is under-predicted if the model parameters used are those fitted to test data over a range of temperatures and optimised for the lower temperature range within which Esshete 1250 is normally operated.

## 7 Acknowledgements

The work reported here is a collaborative effort spread over a number of organisations. The authors are grateful to all the participants in the STYLE Framework 7 project.

Mike Smith and Qingrong Xiong are supported via the EPSRC Fellowship in Manufacturing “A whole-life approach to the development of high integrity welding technologies for Generation IV fast reactors”, EP/L015013/1.

This work is published with the permission of EDF Energy.

## 8 References

- 1 P J Withers, Residual stress and its role in failure, *Rep Prog Phys* **70**(12), 2211-2264 (2007).
- 2 R6, Assessment of the integrity of structures containing defects, EDF Energy (2015).
- 3 BS7910:2013, Guide to methods for assessing the acceptability of flaws in metallic structures, British Standards Institution (2013).
- 4 Fitness for Service, API 579-1/ASME FFS-1, Second Edition (2007).
- 5 P J Bouchard, Code characterisation of weld residual stress levels and the problem of innate scatter, *Int Jnl Press Vess and Piping* **85**(3), 152-165 (2008).
- 6 L-E Lindgren, Computational welding mechanics. Thermomechanical and microstructural simulations, Cambridge, Woodhead Publishing Ltd (2007).
- 7 L-E Lindgren, Finite element modeling and simulation of welding part 2: improved material modelling, *J Therm Stress* **24**, 195-231 (2001).
- 8 P Hurrell, C Watson, P J Bouchard, M C Smith, R J Dennis, N A Leggatt, S K Bate and A Warren, Development of weld modelling guidelines in the UK, ASME PVP 2009, Prague, PVP2009-77540 (2009).
- 9 S Bate and M Smith, Determination of residual stresses in welded components by finite element analysis, *Materials Science and Technology* **32**(14), 1505-1516 (2016).
- 10 P J Withers and H K D H Bhadeshia, Overview - Residual stress part 1 - Measurement techniques, *Materials Science and Technology* **17**(4), 355-365 (2001).
- 11 M B Prime, Cross-Sectional Mapping of Residual Stresses by Measuring the Surface Contour After a Cut, *Journal of Engineering Materials and Technology* **123**(2), 162-168 (2000).
- 12 P Dong and J K Hong, Recommendations for Determining Residual Stresses in Fitness-for-Service Applications, *WRC bulletin* **476**, 1-61 (2002).

- 13 P Dong, On the Mechanics of Residual Stresses in Girth Welds, *Journal of Pressure Vessel Technology* **129**(3), 345-354 (2006).
- 14 P Dong and J K Hong, On the Residual Stress Profiles in New API 579/ASME FFS-1 Appendix E, *Welding in the World* **51**(5), 119-127 (2007).
- 15 P Dong, S Song, J Zhang and M H Kim, On residual stress prescriptions for fitness for service assessment of pipe girth welds, *Int Jnl Press Vess and Piping* **123–124**(0), 19-29 (2014).
- 16 P Dong, S Song and X Pei, An IIW residual stress profile estimation scheme for girth welds in pressure vessel and piping components, *Welding in the World* **60**(2), 283-298 (2016).
- 17 A H Yaghi, T H Hyde, A A Becker, W Sun, G Hilson, S Simandjuntak, P E J Flewitt, M J Pavier and D J Smith, Measuring and modelling residual stresses in butt welded P91 steel pipe including effects of phase transformations, *Energy Materials* **4**(3), 124-132 (2009).
- 18 A H Yaghi, T H Hyde, A A Becker, W Sun, G Hilson, S Simandjuntak, P E J Flewitt, M J Pavier and D J Smith, A Comparison Between Measured and Modeled Residual Stresses in a Circumferentially Butt-Welded P91 Steel Pipe, *Journal of Pressure Vessel Technology* **132**(1), 011206-011206-011210 (2010).
- 19 P J Bouchard, Validated residual stress profiles for fracture assessments of stainless steel pipe girth welds, *Int Jnl Press Vess and Piping* **84**(4), 195-222 (2007).
- 20 R A W Bradford, Through-thickness distributions of welding residual stresses in austenitic stainless steel cylindrical butt welds, *Proceedings of ICRS-6*, 1373-1381.
- 21 D J Smith, P J Bouchard and D George, Measurement and prediction of residual stresses in thick-section steel welds, *The Journal of Strain Analysis for Engineering Design* **35**(4), 287-305 (2000).
- 22 P Dong and J K Hong, Analysis of IIW X/XV RSDP Phase I Round-Robin Residual Stress Results, *Welding in the World* **46**(5), 24-31 (2002).
- 23 J-J Janosch, International Institute of Welding work on residual stress and its application to industry, *Int Jnl Press Vess and Piping* **85**(3), 183-190 (2008).
- 24 P Lindström and L Josefson, 2D, Axisymmetric and 3D Finite Element Analysis Assessment of the IIW RSDP Round Robin Initiative, Phase 1 and Phase 2, *International Institute of Welding Report* (2012).
- 25 M C Smith and A C Smith, NeT bead on plate round robin: Comparison of transient thermal predictions and measurements, *Int Jnl Press Vess and Piping* **86**(1), 96-109 (2009).
- 26 M C Smith and A C Smith, NeT bead on plate round robin: Comparison of residual stress predictions and measurements, *Int Jnl Press Vess and Piping* **86**(1), 79-95 (2009).
- 27 M C Smith, A C Smith, R Wimpory and C Ohms, A review of the NeT Task Group 1 residual stress measurement and analysis round robin on a single weld bead-on-plate specimen, *Int Jnl Press Vess and Piping* **120–121**(0), 93-140 (2014).
- 28 P J Bouchard, The NeT bead on plate benchmark for weld residual stress simulation, *Int Jnl Press Vess and Piping* **86**(1), 31-42 (2009).
- 29 M C Smith and A C Smith, Advances in weld residual stress prediction: A review of the NeT TG4 simulation round robins part 2, mechanical analyses, *Int Jnl Press Vess and Piping* **164**, 130-165 (2018).
- 30 M C Smith and A C Smith, Advances in weld residual stress prediction: A review of the NeT TG4 simulation round robin part 1, thermal analyses, *Int Jnl Press Vess and Piping* **164**, 109-129 (2018).
- 31 M C Smith, O Muránsky, C Austin, P Bendeich and Q Xiong, Optimised modelling of AISI 316L(N) material behaviour in the NeT TG4 international weld simulation and measurement benchmark, *Int Jnl Press Vess and Piping* **164**, 93-108 (2018).
- 32 M C Smith, A C Smith, C Ohms and R C Wimpory, The NeT Task Group 4 residual stress measurement and analysis round robin on a three-pass slot-welded plate specimen, *Int Jnl Press Vess and Piping* **164**, 3-21 (2018).
- 33 M C Smith, S K Bate and P J Bouchard, Simple benchmark problems for finite element weld residual stress simulation, *ASME Pressure Vessels and Piping Conference, Paris, PVP2013-98033* (2013).
- 34 C J Hamelin, O Muránsky, M C Smith, T M Holden, V Luzin, P J Bendeich and L Edwards, Validation of a numerical model used to predict phase distribution and residual stress in ferritic steel weldments, *Acta Materialia* **75**(0), 1-19 (2014).
- 35 M C Smith and O Muránsky, The NeT task group 6 weld residual stress measurement and simulation round robin in alloy 600/82, *ASME Pressure Vessels and Piping Conference, Vancouver, PVP2016-63941* (2016).
- 36 S Marlette, P Freyer, M C Smith, A Goodfellow, X Pitoiset, B Voigt, R Rishel and E J Kingston, Simulation and measurement of through-wall residual stresses in a structural weld overlaid pressurizer nozzle, *ASME PVP 2010, Bellevue, WA, July 18-22 2010, PVP2010-25736* (2010).

- 37 M C Smith, O Muransky, P J Bendeich and L Edwards, The impact of key simulation variables on predicted residual stresses in pressuriser nozzle dissimilar metal weld mock-ups. Part 1 – simulation, ASME PVP 2010, Bellevue, Wa, July 18-22 2010, PVP2010-26023 (2010).
- 38 M C Smith, O Muransky, A Goodfellow, E J Kingston, P Freyer, S Marlette, G Wilkowski, F Brust and D J Shim, The impact of key simulation variables on predicted residual stresses in pressuriser nozzle dissimilar metal weld mock-ups. Part 2 – comparison of simulation and measurements, ASME PVP 2010, Bellevue, Wa., 18-22 July 2010, PVP2010-26025 (2010).
- 39 O Muransky, M C Smith, P J Bendeich and L Edwards, Validated numerical analysis of residual stresses in Safety Relief Valve (SRV) nozzle mock-ups, Computational Materials Science **50**(7), 2203-2215 (2011).
- 40 P J Bendeich, O Muransky, C J Hamelin, M C Smith and L Edwards, Validated numerical analysis of residual stresses in safety relief valve (SRV) nozzle mock-ups: influence of axial restraint on distortion and residual stress predictions, Computational Materials Science **62**, 285-288 (2012).
- 41 H J Rathbun, D Rudland, L Fredette, A Csontos and P Scott, NRC welding residual stress validation program – International round robin details and findings, 2011 ASME Pressure Vessels and Piping Division Conference, Baltimore, 17th-20th July 2011, PVP 2011-57642 (2011).
- 42 L Fredette, M Kerr, H J Rathbun and J E Broussard, NRC/EPRI Welding Residual Stress Validation Program - Phase III Details and Findings, ASME Pressure Vessels and Piping Conference, Baltimore, PVP2011-57645 (2011).
- 43 P Dong and J K Hong, Analysis of IIW X/XV RSDP Phase I round-robin residual stress results, Welding in the World **46**(5/6), 24-31 (2002).
- 44 A H Mahmoudi, S Hossain, C E Truman, D J Smith and M J Pavier, A new procedure to measure near yield residual stresses using the deep hole drilling technique, Experimental Mechanics **49**(4), 595-604 (2008).
- 45 M C Smith, A C Smith and T Nicak, Final Report of the STYLE project, European Commission Seventh Framework Programme Report (2014).
- 46 C Austin and L A Higham, A Constitutive Model for Parent Esshete 1250 and Associated Single Bead Weld Metal, Serco Assurance Report SA/SIA/17261/R01, Issue 1 (2008).
- 47 M C Smith, O Muransky, Q Xiong and C Austin, Validated prediction of weld residual stresses in austenitic steel pipe girth welds before and after thermal ageing, Part 1: mock-up manufacture, residual stress measurements, and materials characterisation, Submitted to International Journal of Pressure Vessels and Piping, (2019).
- 48 O Muransky, M C Smith, P J Bendeich, C J Hamelin and L Edwards, Prediction and measurement of weld residual stresses in thermally aged girth-welded austenitic steel pipes, ASME pressure vessels and piping conference, Toronto, PVP2102-78409 (2012).
- 49 ABAQUS/Standard User's Manual, Version 6.9, Providence, RI, Simulia (2009).
- 50 R M Smith, FEAT-WMT: weld-modelling tool user guide FEATPLUS Limited Report FP/CR/0029/11 (2011).
- 51 P J Bouchard, Residual Stress Simulation Heat Input Models for Stainless Steel Manual Metal Arc Welds, British Energy Report E/REP/BDBB/0009/GEN/03, Revision 000 (2003).
- 52 J Lemaitre and J L Chaboche, Mechanics of Solid Materials, Cambridge University Press (1990).
- 53 O Muransky, C J Hamelin, M C Smith, P J Bendeich and L Edwards, The effect of plasticity theory on predicted residual stress fields in numerical weld analyses, Computational Materials Science **54**, 125-134 (2011).
- 54 M C Smith, P J Bouchard, M Turski, L Edwards and R J Dennis, Accurate prediction of residual stress in stainless steel welds, Computational Materials Science **54**, 312-328 (2012).
- 55 L Vaughn, Esshete 1250 Material Modelling: Generalised Abaqus Creep Subroutines, Frazer-Nash Consultancy Report FNC 32213/001/31492R, Issue 1 (2006).
- 56 C E Truman and M C Smith, The NeT residual stress measurement and analysis round robin on a single weld bead-on-plate specimen, Int Jnl Press Vess and Piping **86**(1), 1-2 (2009).
- 57 O Muransky, M C Smith, P J Bendeich, T M Holden, V Luzin, R V Martins and L Edwards, Comprehensive numerical analysis of a three-pass bead-in-slot weld and its critical validation using neutron and synchrotron diffraction residual stress measurements, International Journal of Solids and Structures **49**(9), 1045-1062 (2012).

## 9 Tables

Table 1: Thermo-physical and physical properties of Esshete 1250

| Temp.              | Specific Heat <sup>a</sup>                    | Conductivity                                | Thermal Expansion <sup>b</sup><br>$10^{-6}$   | Parent Young's Modulus | Weld Young's Modulus <sup>d</sup> | Poisson's Ratio |
|--------------------|---|---|---|------------------------|-----------------------------------|-----------------|
| $^{\circ}\text{C}$ | $\frac{\text{kJ}}{\text{kg}^{\circ}\text{C}}$ | $\frac{\text{W}}{\text{m}^{\circ}\text{C}}$ | $\frac{\text{mm}}{\text{mm}^{\circ}\text{C}}$ | GPa                    | GPa                               |                 |
| 20                 | 0.490   | 12.69                                       | 15.44   | 204.5                  | 157.8                             | 0.294           |
| 100                | 0.508   | 13.93                                       | 16.01   | 196.7                  | 151.5                             | 0.294           |
| 200                | 0.532   | 15.48                                       | 16.67   | 188.1                  | 144.4                             | 0.294           |
| 300                | 0.555   | 17.03                                       | 17.29   | 180.2                  | 137.8                             | 0.294           |
| 400                | 0.580   | 18.58                                       | 17.87   | 172.5                  | 131.4                             | 0.294           |
| 500                | 0.603   | 20.13                                       | 18.41   | 164.6                  | 124.8                             | 0.294           |
| 600                | 0.627   | 21.68                                       | 18.91   | 156.0                  | 117.7                             | 0.294           |
| 700                | 0.650   | 23.23                                       | 19.37   | 146.1                  | 109.8                             | 0.294           |
| 800                | 0.650   | 24.78                                       | 19.78   | 134.6                  | 100.6                             | 0.294           |
| 900                | 0.650   | 26.33                                       | 20.16   | 120.8                  | 89.9                              | 0.294           |
| 1000               | 0.650   | 27.88                                       | 20.49   | 104.4                  | 77.4                              | 0.294           |
| 1100               | 0.650   | 29.43                                       | 20.78   | 84.8                   | 62.6                              | 0.294           |
| 1200               | 0.650   | 30.98                                       | 21.03   | 61.5                   | 45.3                              | 0.294           |
| 1300               | 0.650   | 32.53                                       | 21.24   | 34.1                   | 25.0                              | 0.294           |
| 1400 <sup>c</sup>  | 0.650   | 34.08                                       | 21.41   | 2.0                    | 1.6                               | 0.294           |

- a) Specific heat capacity values are instantaneous data  
 b) Thermal expansion values represent the mean linear coefficient of expansion from 20°C to temperature  
 c) Solidus temperature = 1375°C; Liquidus temperature = 1400°C

Density = 7960 kg/m<sup>3</sup> at 20°C

Table 2: Lemaitre-Chaboche parameter fits to Esshete 1250 parent material behaviour

| Model ID       | Description   |
|----------------|---|
| Parent model 1 | Historical model, with kinematic parameters fitted to monotonic and first quarter cycle of 1.5% TSR cyclic test data, using a single back-stress, and with $Q_{inf}$ increased to match the cyclic hardening behaviour of 2.5% TSR cyclic tests |
| Parent model 2 | Kinematic parameters fitted to monotonic loading with two back-stresses, with $Q_{inf}$ increased to match the cyclic hardening behaviour of 2.5% TSR cyclic tests  |
| Parent model 3 | Kinematic parameters fitted to monotonic loading with two back-stresses, with $Q_{inf}$ fitted to match the cyclic hardening behaviour of 1.5% TSR cyclic tests   |
| Parent model 4 | Kinematic parameters fitted to first re-loading from compression in cyclic tests, with two back-stresses, with $Q_{inf}$ increased to match the cyclic hardening behaviour of 2.5% TSR cyclic tests   |
| Parent model 5 | Kinematic parameters fitted to first re-loading from compression in cyclic tests, with two back-stresses, with $Q_{inf}$ fitted to match the cyclic hardening behaviour of 1.5% TSR cyclic tests  |

Table 3: Lemaitre-Chaboche parameter fits to Esshete 1250 weld metal behaviour

| Model ID     | Description   |
|--------------|---|
| Weld model 1 | Historical model, fitted to single-pass MMA weld metal data using a single back-stress, and with $Q_{inf}$ increased to saturate at the 0.2% proof stress of multi-pass weld metal  |
| Weld model 2 | Kinematic parameters fitted to monotonic loading with two back-stresses, with $Q_{inf}$ increased to saturate at the 0.2% proof stress of multi-pass weld metal   |
| Weld model 3 | Kinematic parameters fitted to monotonic loading with two back-stresses, with no increase to $Q_{inf}$  |
| Weld model 4 | Kinematic parameters fitted to first re-loading from compression, with two back-stresses, with $Q_{inf}$ increased to saturate at the 0.2% proof stress of multi-pass weld metal  |
| Weld model 5 | Kinematic parameters fitted to first re-loading from compression, with two back-stresses, with no increase to $Q_{inf}$   |
| Weld model 6 | Kinematic parameters fitted to first re-loading from compression, with two back-stresses, with $\sigma_0$ reduced to simulate as-deposited weld metal, and with $Q_{inf}$ increased further to still saturate at the 0.2% proof stress of multi-pass weld metal   |
| Weld model 7 | Kinematic parameters fitted to first re-loading from compression, with two back-stresses, with $\sigma_0$ reduced to simulate as-deposited weld metal, and with $Q_{inf}$ increased to saturate at the test levels (ie not MP yield strength)   |
| Weld model 8 | Kinematic parameters fitted to first re-loading from compression, with two back-stresses, with $\sigma_0$ reduced to simulate as-deposited weld metal, with $Q_{inf}$ increased further to saturate at the 0.2% proof stress of multi-pass weld metal, and with reduced $\mathbf{b}$ at RT and 200°C      |
| Weld model 9 | Kinematic parameters fitted to first re-loading from compression, with two back-stresses, with $\sigma_0$ reduced to simulate as-deposited weld metal, with $Q_{inf}$ increased further to saturate at the 0.2% proof stress of multi-pass weld metal, and with $\mathbf{b}$ halved again at RT and 200°C |

Table 4: Creep deformation coefficients for Eshete 1250 using the RCC-MR type creep deformation model

| Model     | $C_1$                                  | $C_2$  | n      | C                                      | $n_1$  |
|-----------|--|--------|--------|--|--------|
| Baseline  | $4.3783 \times 10^{-8} \exp(-24301/T)$ | 0.4696 | 7.0969 | $3.0578 \times 10^{-8} \exp(-41075/T)$ | 8.9395 |
| Optimised | $4.3783 \times 10^{-8} \exp(-24301/T)$ | 0.4696 | 7.0969 | $3.0578 \times 10^{-8} \exp(-41075/T)$ | 9.9395 |

Table 5: Modelled weld process parameters for Weld 5 in pipe CY7/CY6

| Pass | process | wire/elec dia | Layer | V    | I   | v      | VI/v    | Efficiency | correlation bead area | ABAQUS bead area | ratio   | Melted area | Source radius (all) | Horizontal weave amplitude |
|------|---------|---------------|-------|------|-----|--------|---------|------------|-----------------------|------------------|---------|-------------|---------------------|----------------------------|
|      |         | (mm)          |       | (V)  | (A) | (mm/s) | kJ/mm   |            |                       |                  |         |             | (mm)                | (mm)                       |
| 1    | TIG     | 2.4           | root  | 9.7  | 86  | 0.85   | 0.98    | 85%        | 14.72                 | 15.3             | 104%    | 142%        | 2.4                 | 4.5                        |
| 2    | TIG     | 2.4           | 1     | 10.6 | 102 | 1.25   | 0.86    | 95%        | 12.97                 | 13.5             | 104%    | 249%        | 1.8                 | 4.5                        |
| 3    | MMA     | 3.2           | 2     | 25.7 | 121 | 2.24   | 1.39    | 75%        | 20.82                 | 21.56            | 104%    | 205%        | 3.2                 | 4.5                        |
| 4    | MMA     | 3.2           | 2     | 26.9 | 120 | 2.32   | 1.39    | 80%        | 20.87                 | 21.56            | 103%    | 197%        | 3.2                 | 4.5                        |
| 5    | MMA     | 3.2           | 3     | 26.2 | 118 | 2.07   | 1.49    | 82%        | 22.40                 | 23.27            | 104%    | 200%        | 3.2                 | 4.5                        |
| 6    | MMA     | 3.2           | 3     | 27.1 | 119 | 2.16   | 1.49    | 85%        | 22.40                 | 23.27            | 104%    | 204%        | 3.2                 | 4.5                        |
| 7    | MMA     | 4             | 4     | 26   | 159 | 2.37   | 1.74    | 78%        | 26.16                 | 27.23            | 104%    | 197%        | 4                   | 4.5                        |
| 8    | MMA     | 4             | 4     | 26.3 | 162 | 2.44   | 1.75    | 80%        | 26.19                 | 27.23            | 104%    | 201%        | 4                   | 4.5                        |
| 9    | MMA     | 4             | 5     | 26.8 | 160 | 2.46   | 1.74    | 75%        | 26.15                 | 27.72            | 106%    | 197%        | 4                   | 4.5                        |
| 10   | MMA     | 4             | 5     | 26.2 | 159 | 2.39   | 1.74    | 80%        | 26.15                 | 27.72            | 106%    | 198%        | 4                   | 4.5                        |
| 11   | MMA     | 4             | 6     | 26.8 | 161 | 2.47   | 1.75    | 75%        | 26.20                 | 27.41            | 105%    | 202%        | 4                   | 4.5                        |
| 12   | MMA     | 4             | 6     | 26.4 | 161 | 2.44   | 1.74    | 78%        | 26.13                 | 27.41            | 105%    | 197%        | 4                   | 4.5                        |
| 13   | MMA     | 4             | 7     | 26.1 | 161 | 2.41   | 1.74    | 75%        | 26.15                 | 27.1             | 104%    | 205%        | 4                   | 4.5                        |
| 14   | MMA     | 4             | 7     | 25.9 | 161 | 2.39   | 1.74    | 80%        | 26.17                 | 27.1             | 104%    | 201%        | 4                   | 5                          |
| 15   | MMA     | 5             | 8     | 26.3 | 200 | 2.90   | 1.81    | 79%        | 27.21                 | 30.16            | 111%    | 197%        | 5                   | 5                          |
| 16   | MMA     | 5             | 8     | 26.9 | 198 | 2.94   | 1.81    | 83%        | 27.17                 | 30.16            | 111%    | 197%        | 5                   | 5                          |
| 17   | MMA     | 5             | 9     | 26.4 | 199 | 2.90   | 1.81    | 78%        | 27.17                 | 30.42            | 112%    | 199%        | 5                   | 5                          |
| 18   | MMA     | 5             | 9     | 26.1 | 200 | 2.88   | 1.81    | 85%        | 27.19                 | 30.42            | 112%    | 200%        | 5                   | 5.5                        |
| 19   | MMA     | 5             | 10    | 26.7 | 198 | 2.92   | 1.81    | 76%        | 27.16                 | 29.5             | 109%    | 197%        | 5                   | 5.5                        |
| 20   | MMA     | 5             | 10    | 25.9 | 199 | 2.85   | 1.81    | 82%        | 27.13                 | 29.5             | 109%    | 202%        | 5                   | 5.5                        |
| 21   | MMA     | 5             | 11    | 26.9 | 199 | 2.96   | 1.81    | 74%        | 27.13                 | 31.42            | 116%    | 203%        | 5                   | 5.5                        |
| 22   | MMA     | 5             | 11    | 25.5 | 199 | 2.80   | 1.81    | 79%        | 27.18                 | 31.42            | 116%    | 198%        | 5                   | 5.5                        |
| 23   | MMA     | 5             | cap   | 25.9 | 200 | 2.10   | 2.47    | 64%        | 37.00                 | 38.29            | 103%    | 199%        | 5                   | 6.5                        |
| 24   | MMA     | 5             | cap   | 25.8 | 201 | 2.17   | 2.39    | 74%        | 35.85                 | 38.29            | 107%    | 196%        | 5                   | 6.5                        |
|      |         |               |       |      |     |        | average | 79%        |                       |                  | average | 199%        |                     |                            |

*Table 6: Matrix of phase 2 material property sensitivity studies*

| <b>Case</b> | <b>Parent model</b> | <b>Weld model</b> |
|-------------|---------------------|-------------------|
| mech 1      | model 4             | model 5           |
| mech 2      | model 4             | model 6           |
| mech 4      | model 2             | model 6           |
| kine        | model 2             | model 6           |
| mech 5      | model 2             | model 4           |
| mech 6      | model 2             | model 5           |
| mech 7      | model 2             | model 7           |
| mech 8      | model 4             | model 4           |
| mech 9      | model 4             | model 7           |
| iso 2       | model 2             | model 6           |
| mech 10     | Model 2             | Model 8           |
| mech 11     | Model 2             | Model 9           |

## 10 Figures

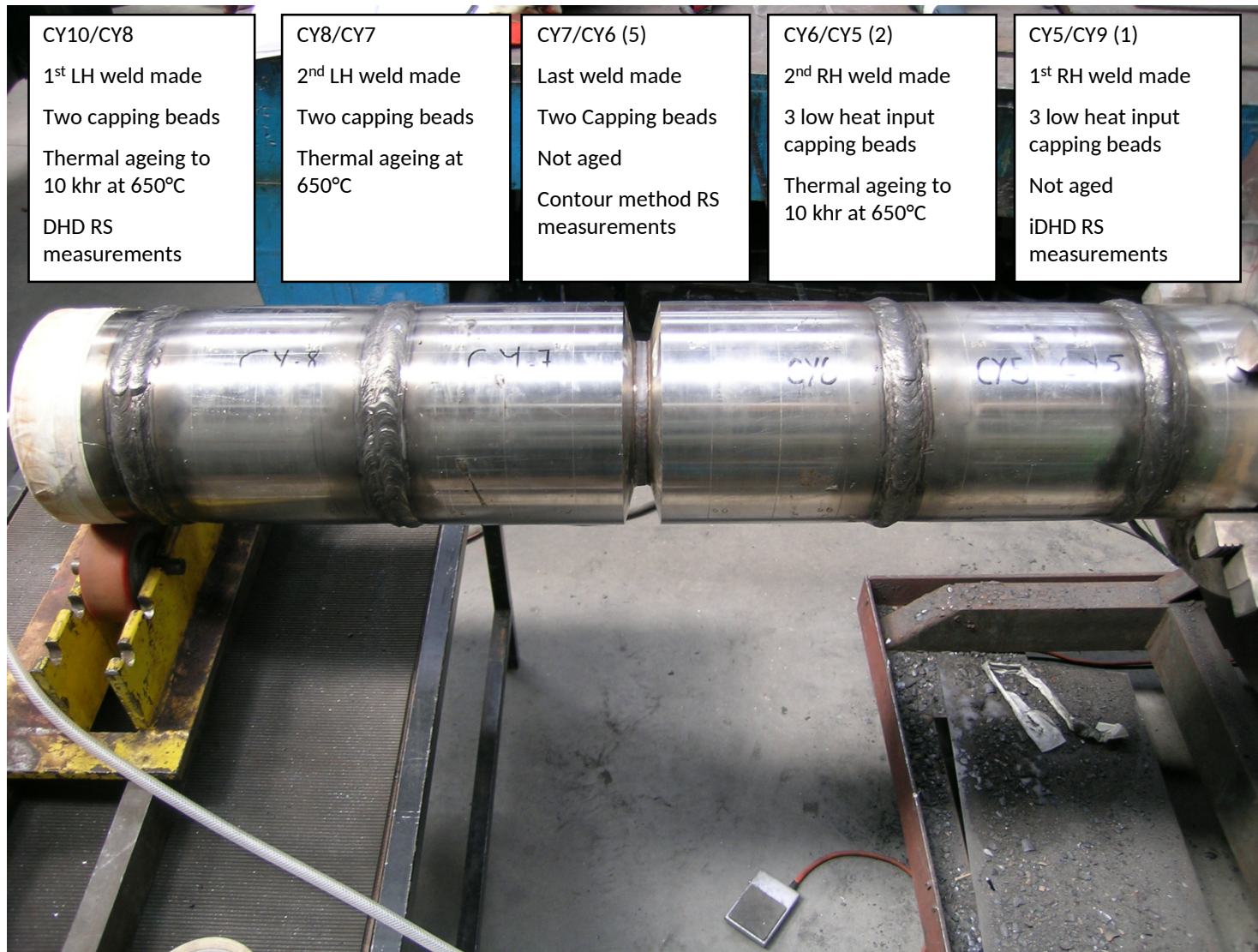


Figure 1: Showing the pipe assembly after completion of the root pass of the last girth weld (CY7/CY6)

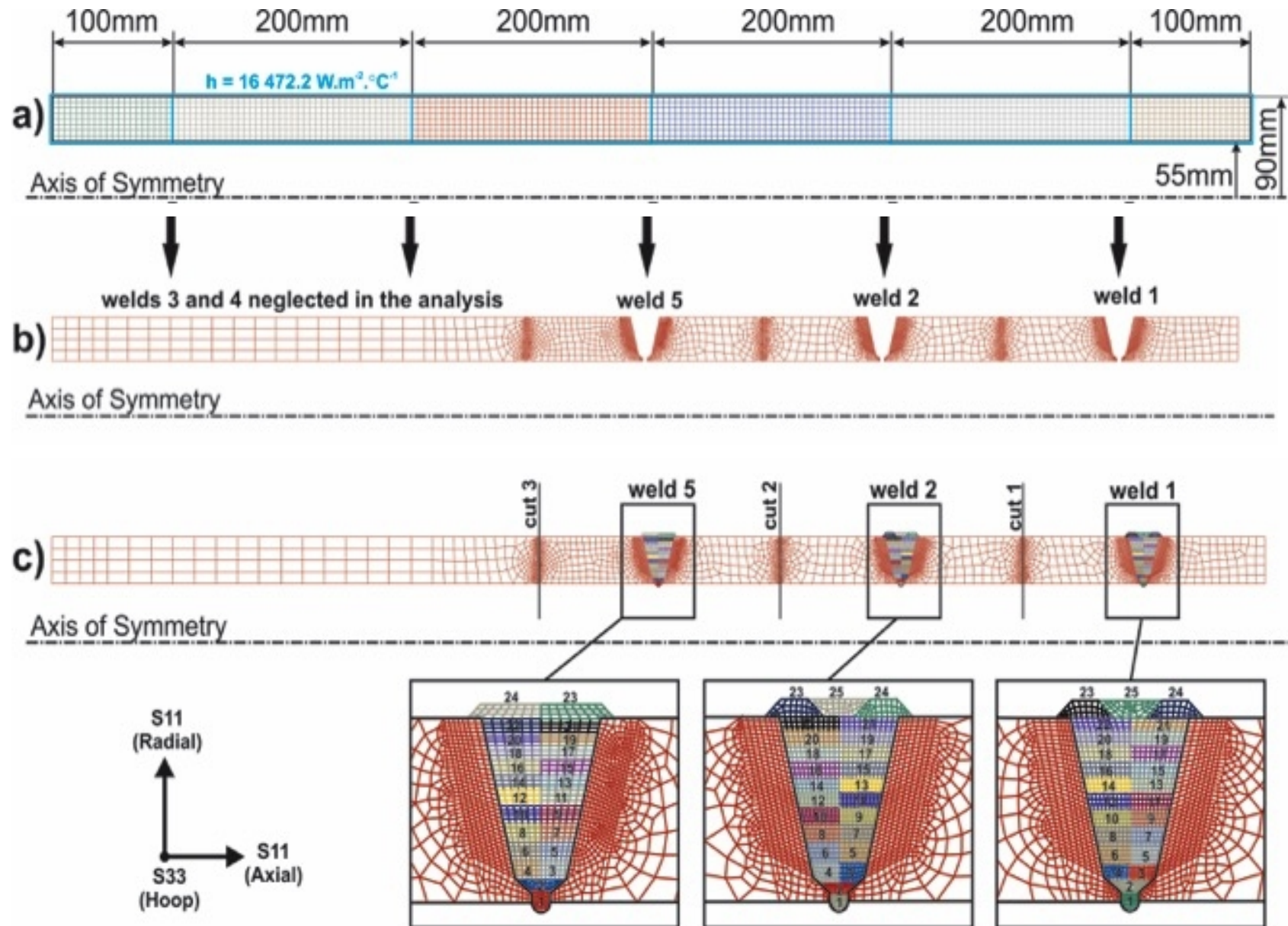


Figure 2: Showing the mesh designs and modelling sequence adopted for the Phase 1 simulations that included the entire manufacturing history (after [48])

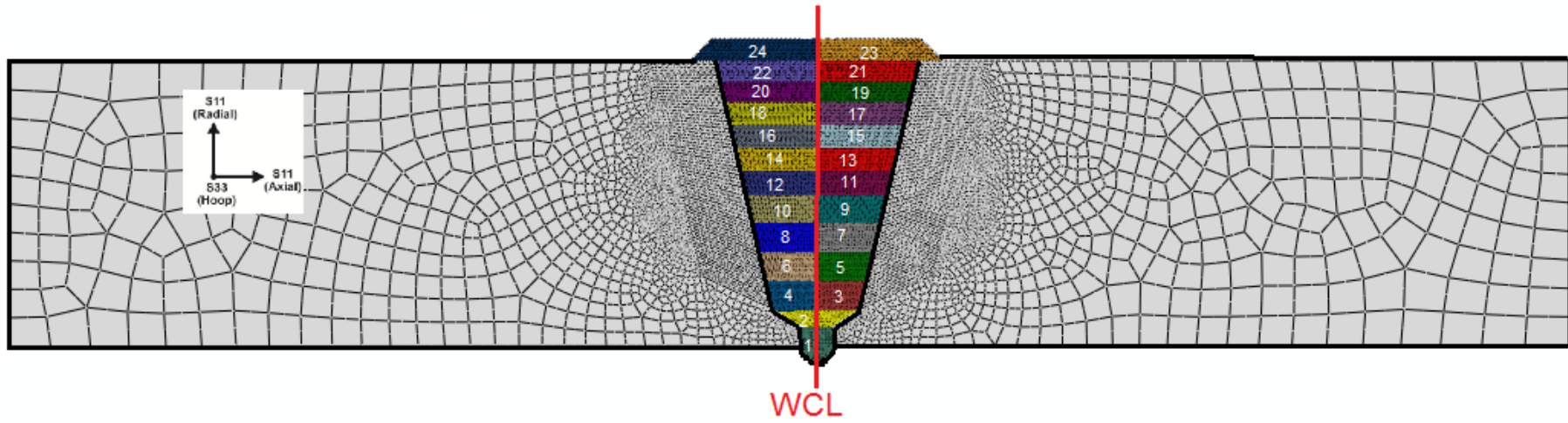


Figure 3: Showing the refined axi-symmetric mesh of pipe CY7/CY6 used for Phase 2 analyses



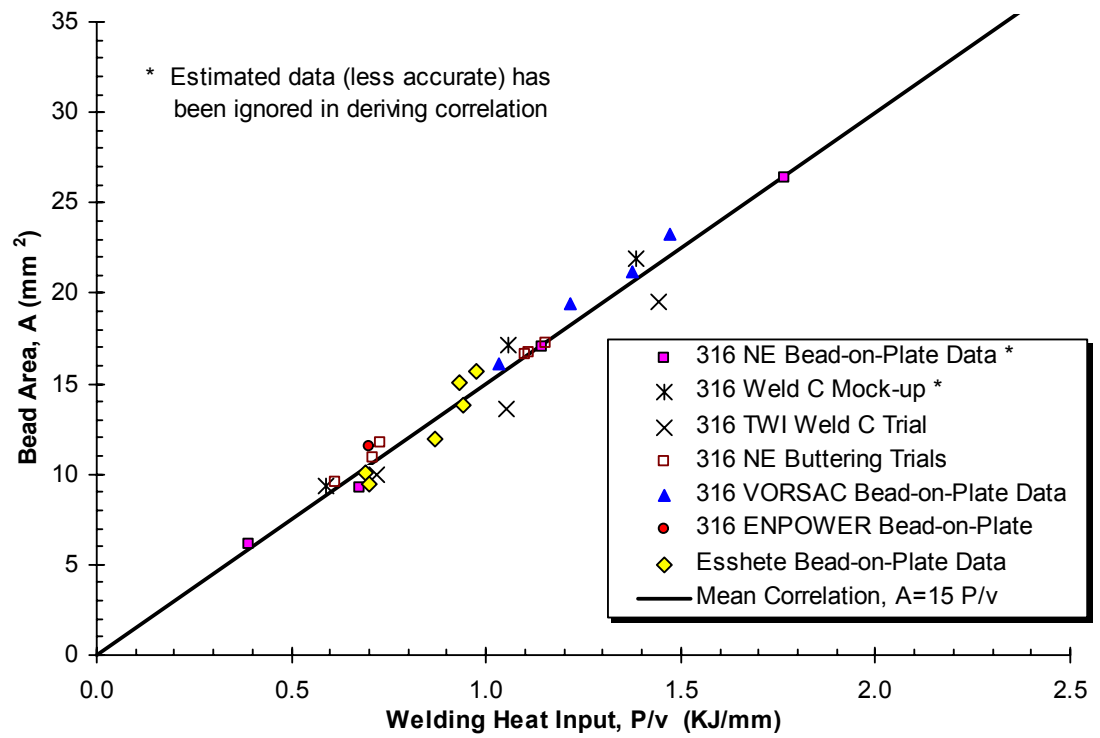


Figure 5: Electrical heat input vs weld filler metal correlation for AISI Type 316 and Esshete 1250 stainless steel MMA weld metal (after[19])

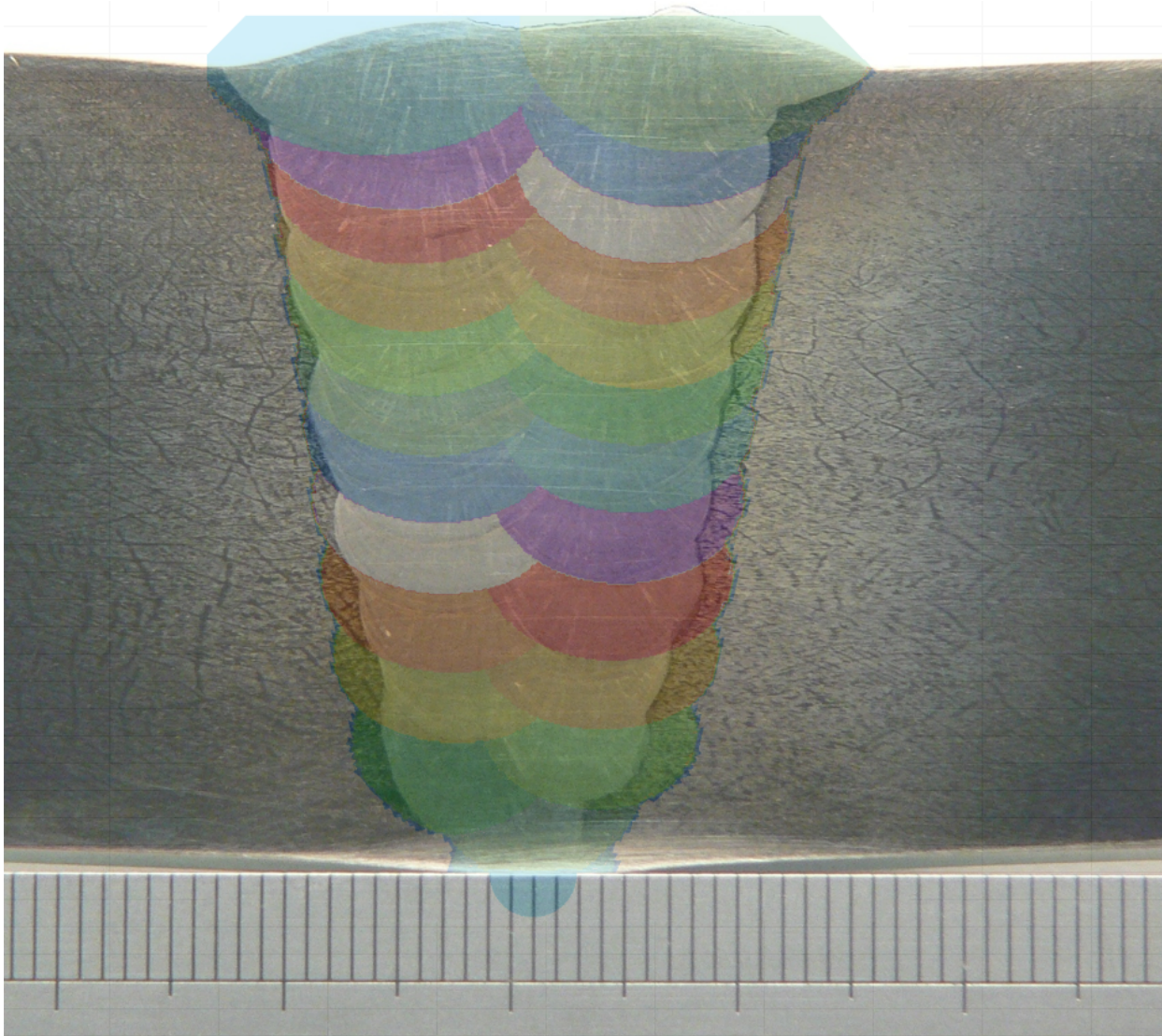


Figure 6: Transverse fusion boundary profile from FE simulation using FEAT/WMT superposed on transverse macrograph of weld CY7/CY6 (note: simulation results flipped about vertical axis to match bead lay-up in macrograph).

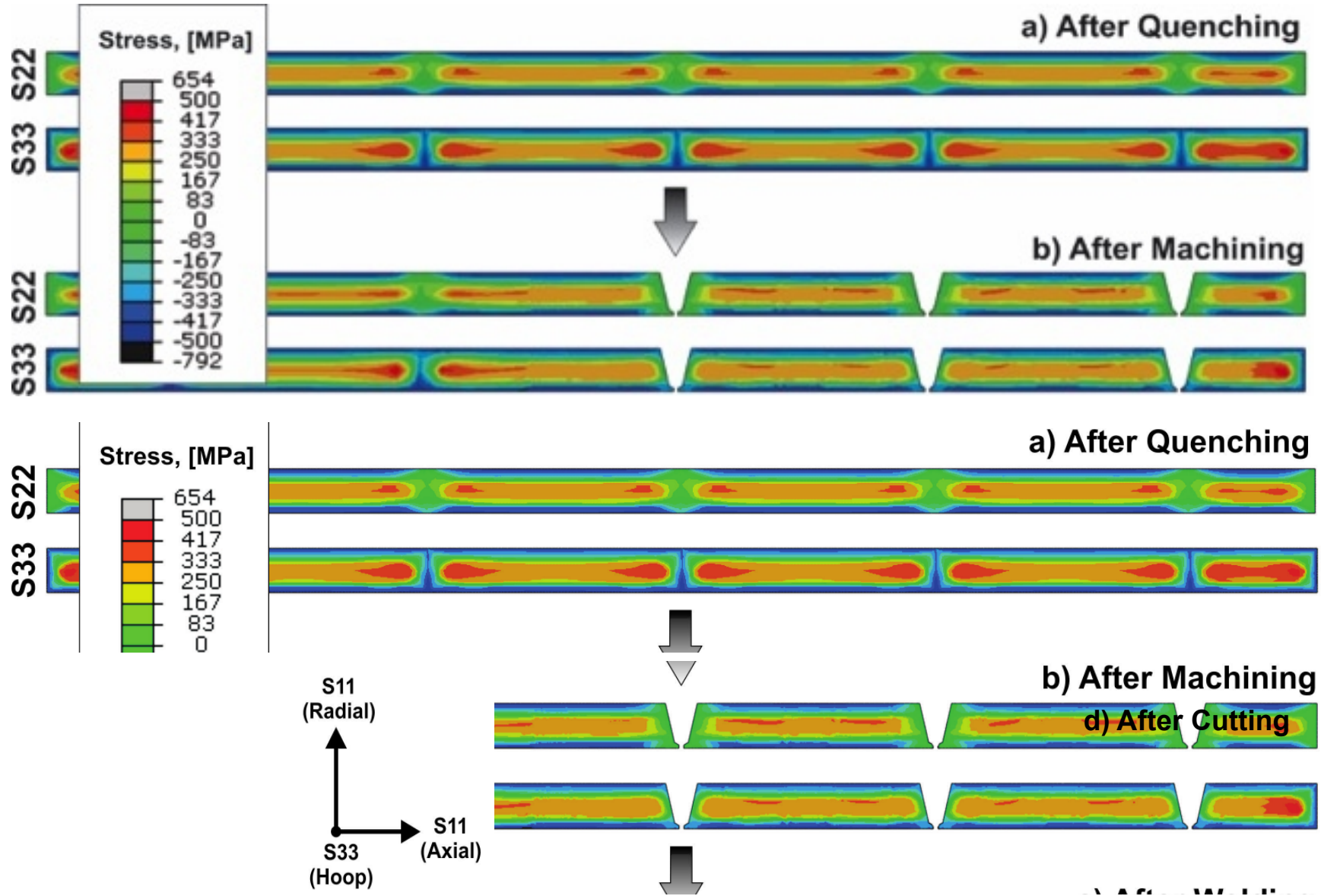
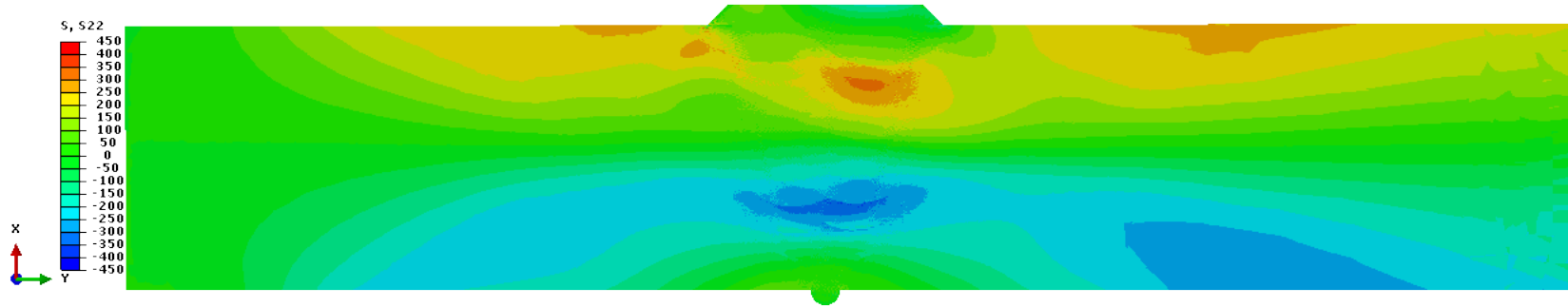
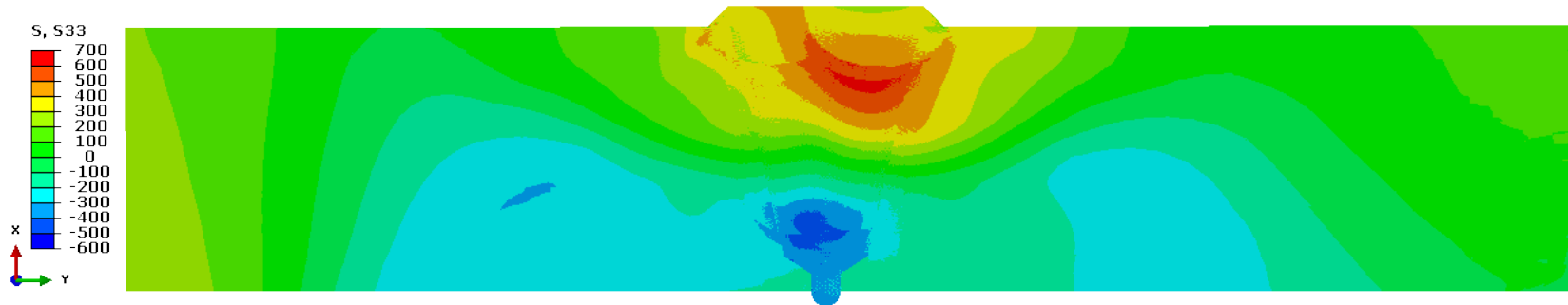


Figure 7: Showing residual stress development during girth-welded pipe manufacture: after quenching (a), after machining (b), after welding (c), and after cutting and root removal (d)



(a) Axial Stress



(b) Hoop stress

Figure 8: Typical as-welded residual stress distribution for two-capping pass weld prior to root machining, with no prior manufacturing history

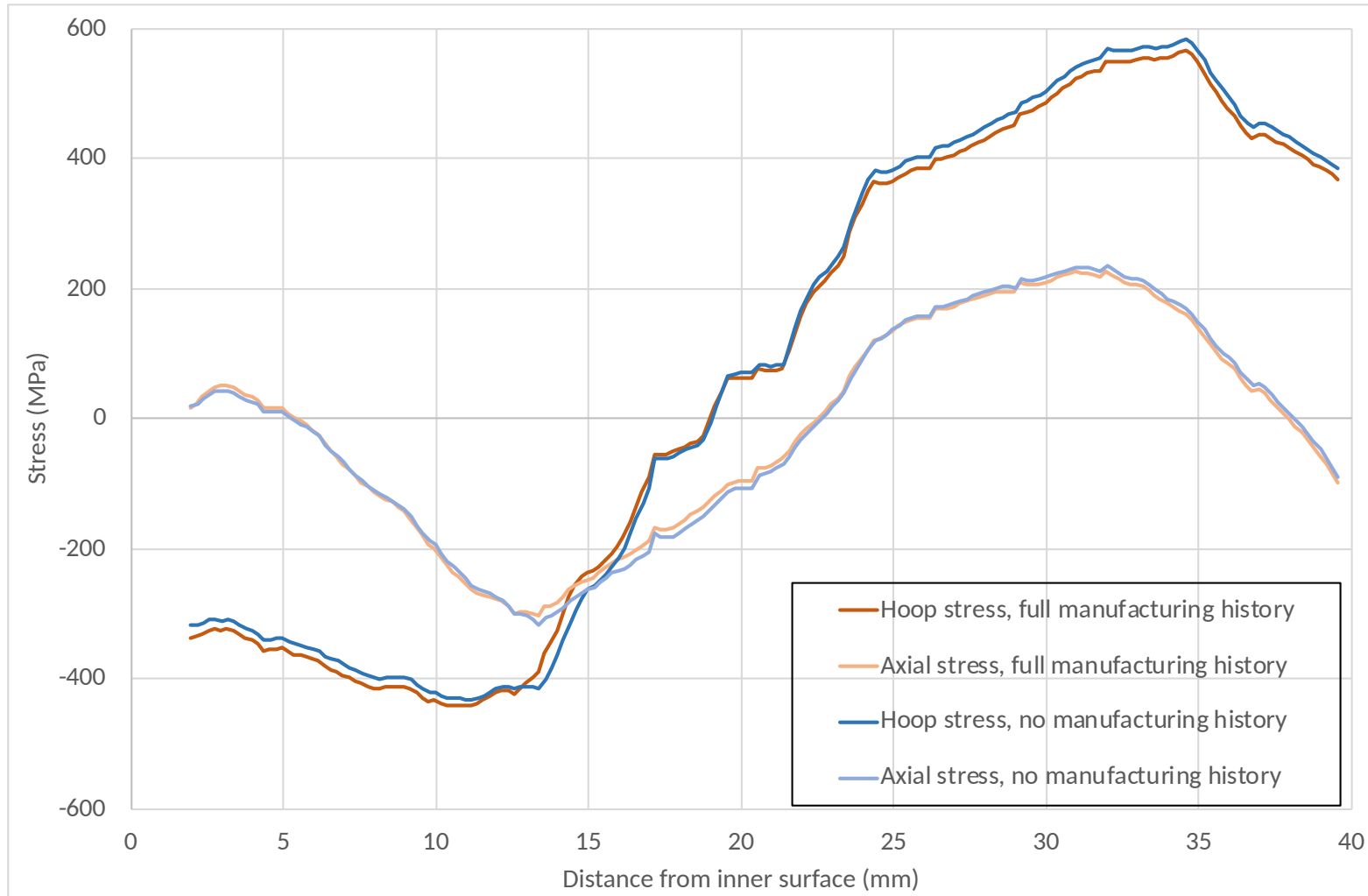


Figure 9: Showing the effect of manufacturing history on predicted stresses at the weld centreline for two-capping pass weld CY7/CY6 (weld 5)

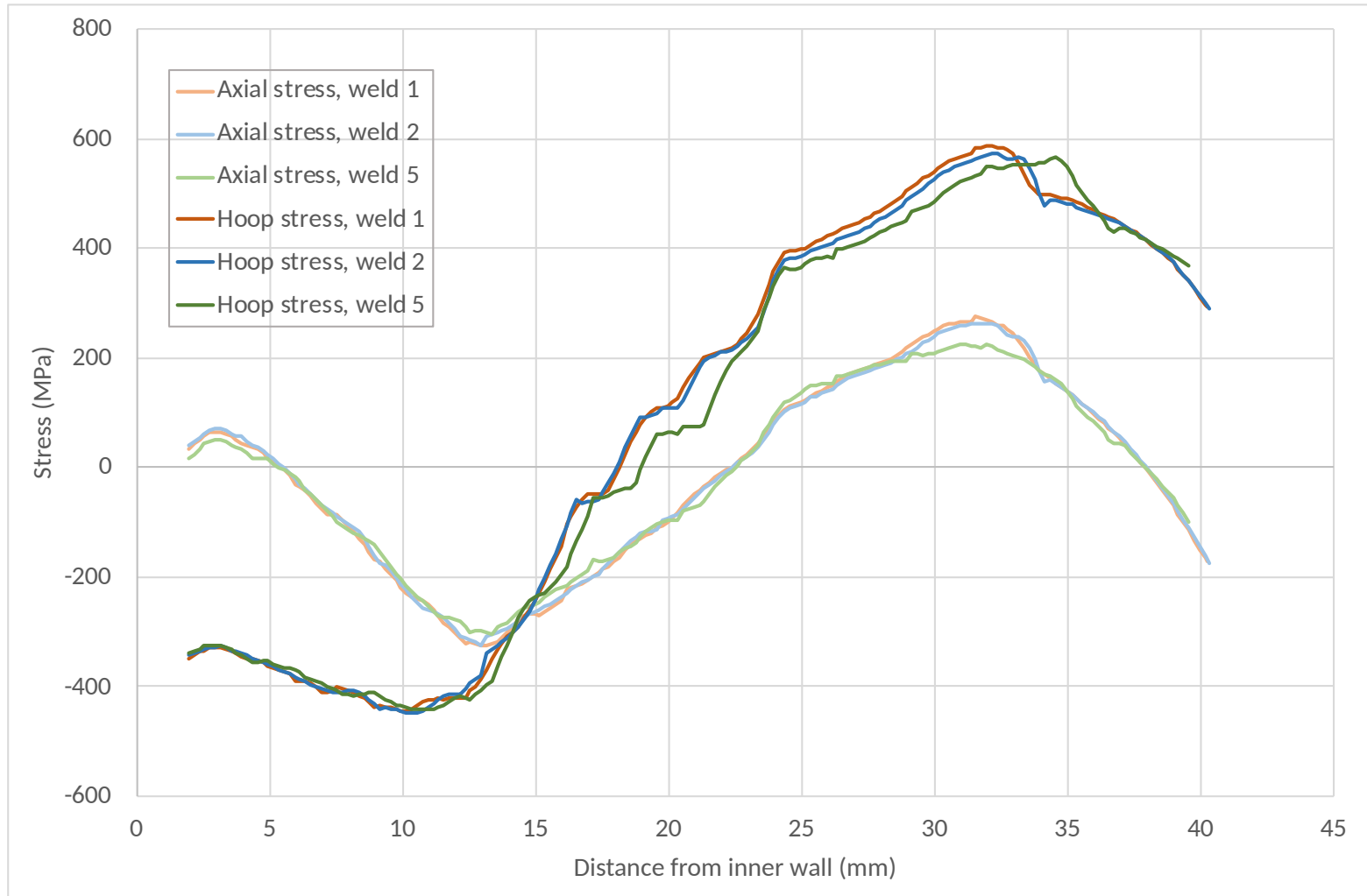


Figure 10: Showing the effect of weld position and capping pass layout on predicted stresses at the weld centreline, full manufacturing history

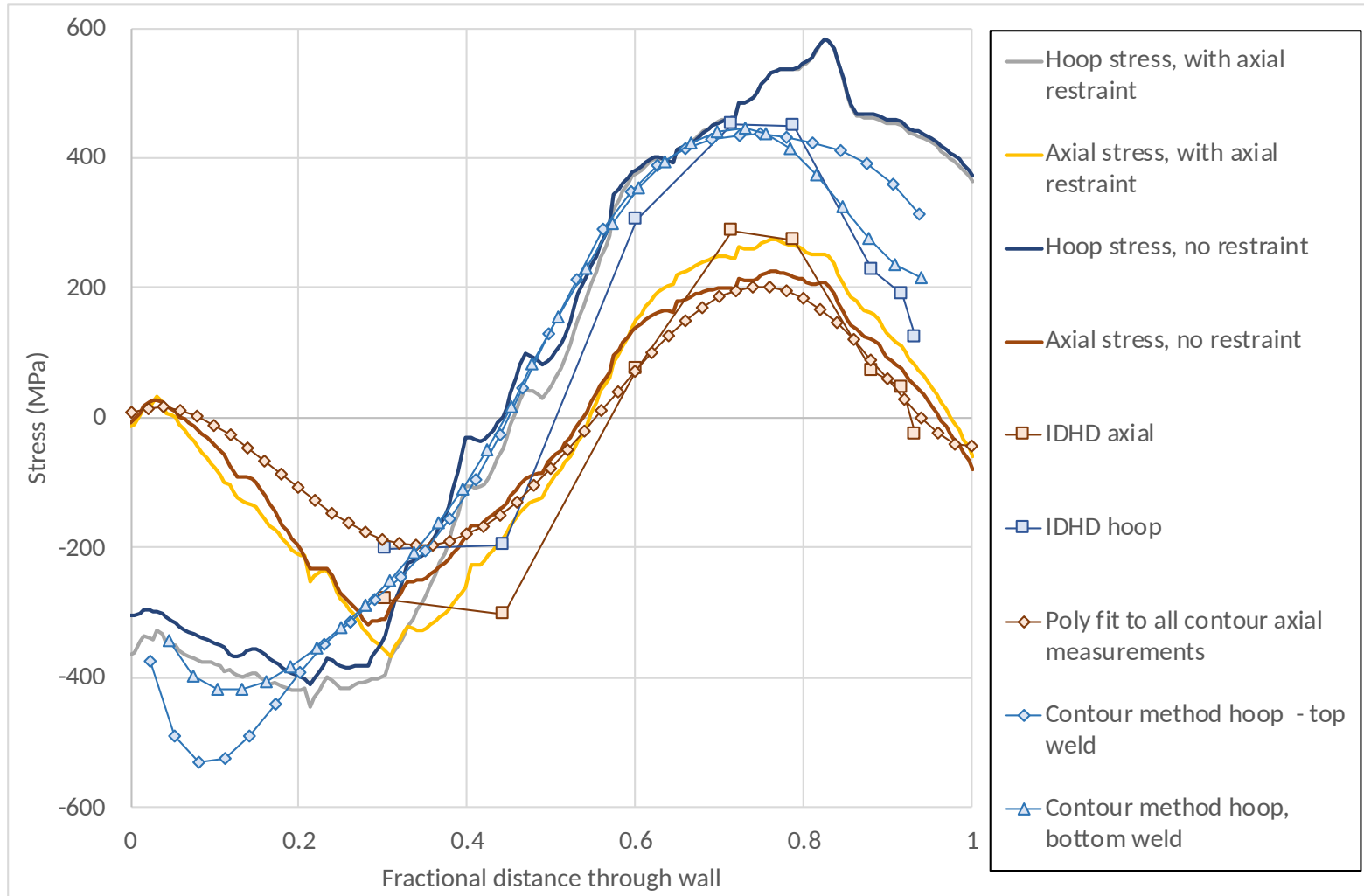


Figure 11: Showing the effect of axial restraint on predicted stresses at the weld centreline, full manufacturing history, compared with iDHD and contour method measurements.

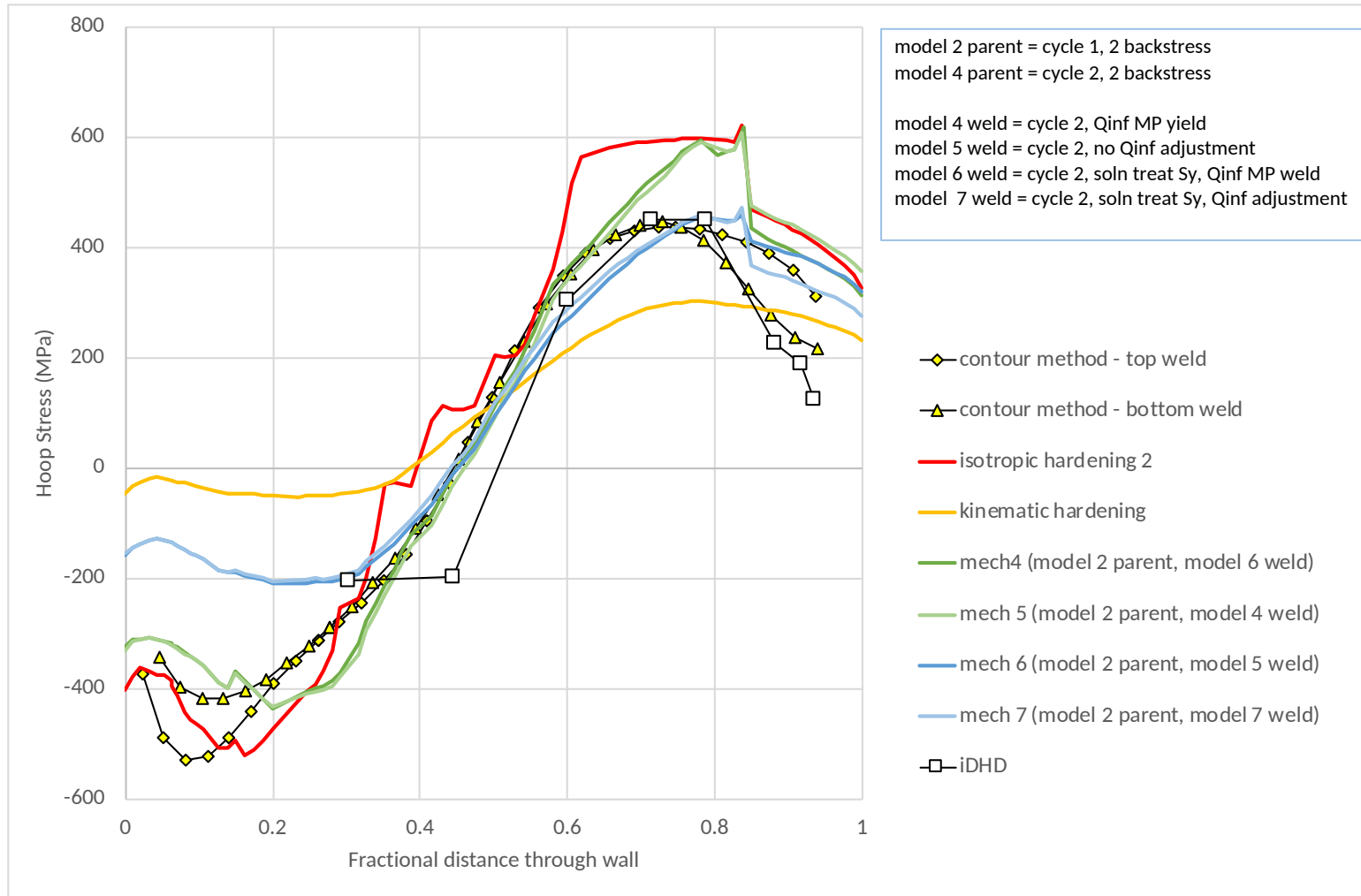


Figure 12: Showing the impact of basic hardening model and weld mixed hardening model initial and saturated conditions on hoop stresses on the weld centreline

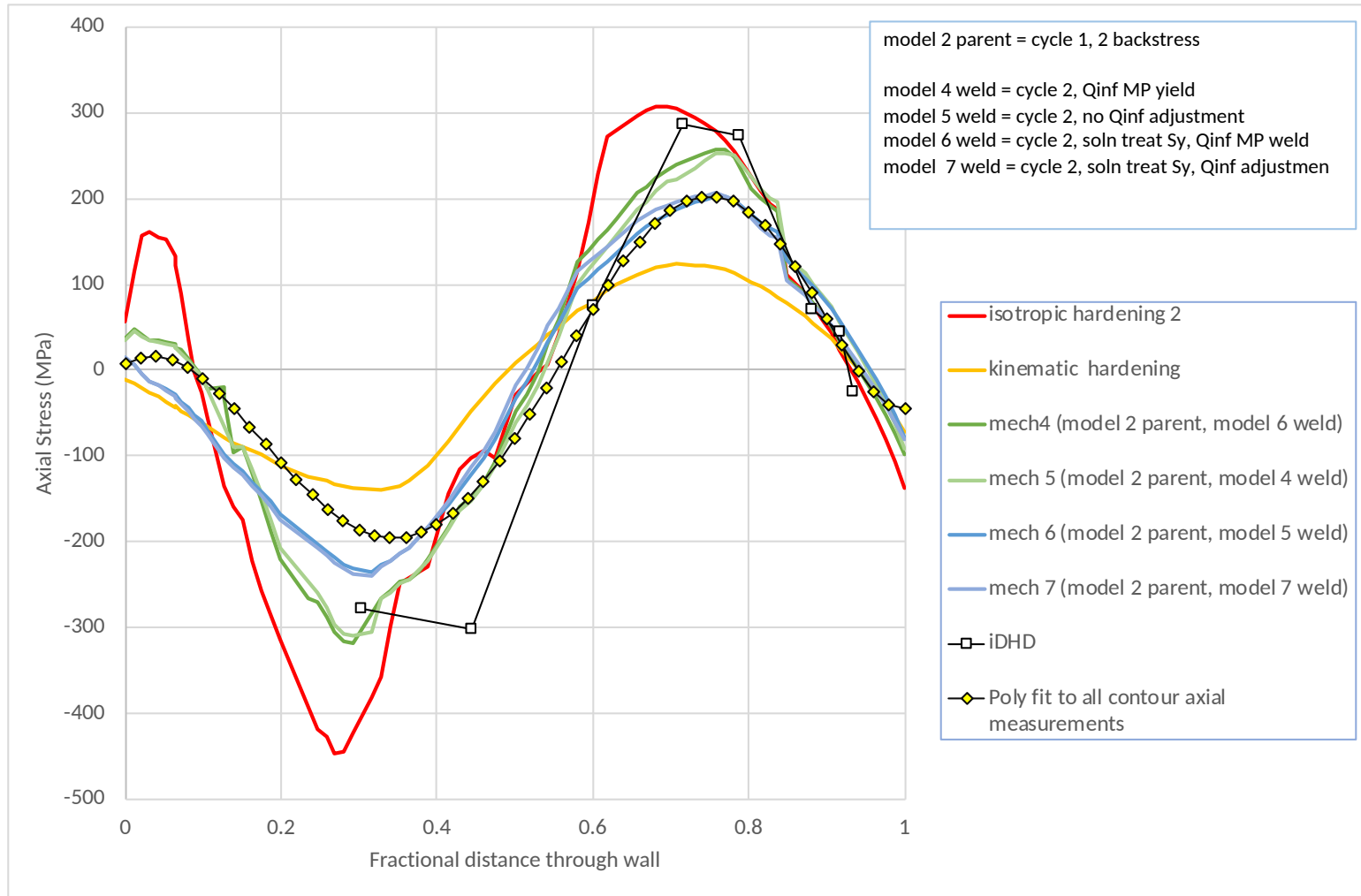


Figure 13: Showing the impact of basic hardening model and weld mixed hardening model initial and saturated conditions on axial stresses on the weld centreline

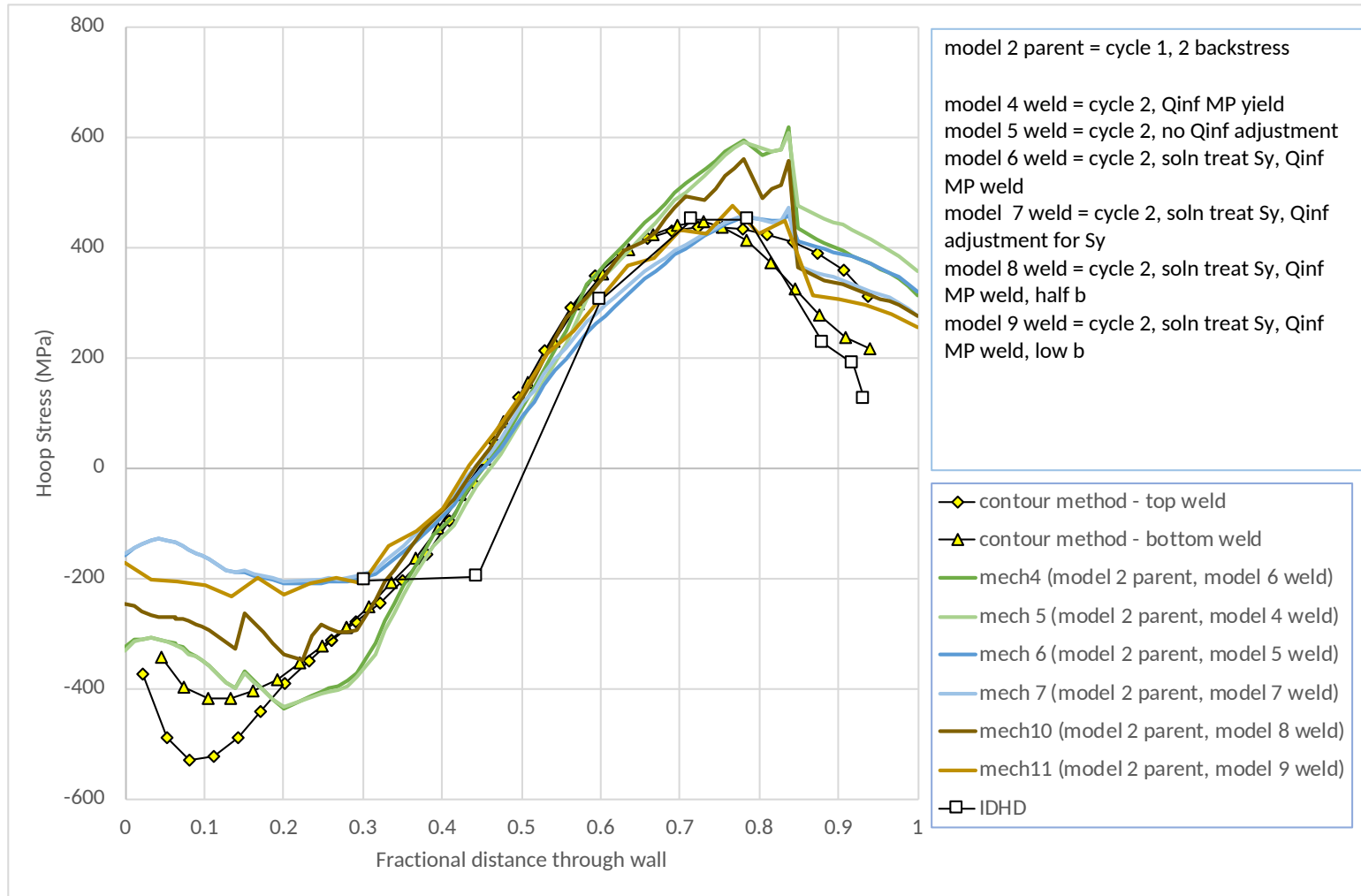


Figure 14 Showing the effect of weld metal starting yield strength and cyclic hardening behaviour on weld centreline hoop stresses

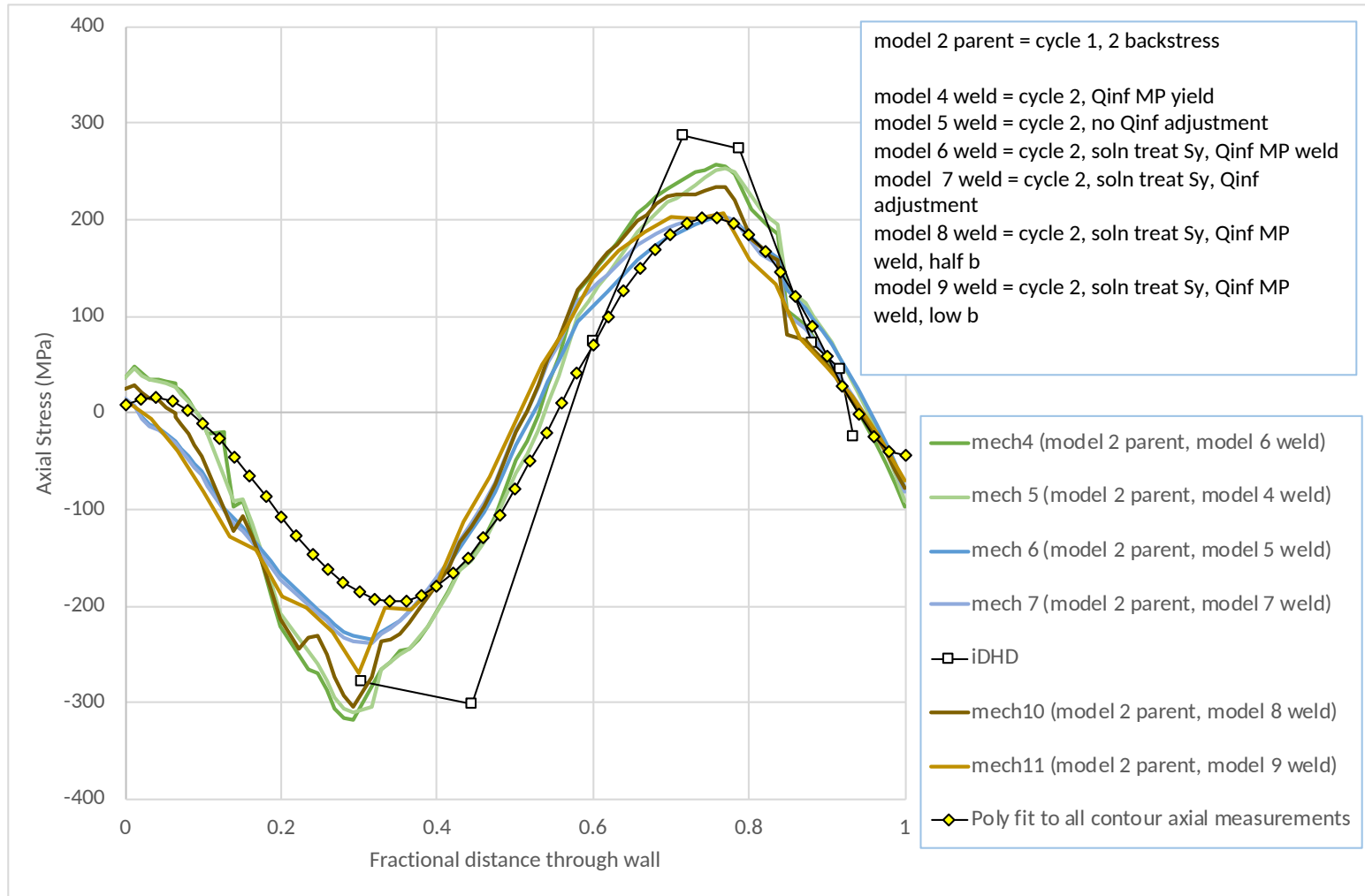


Figure 15 Showing the effect of weld metal starting yield strength and cyclic hardening behaviour on weld centreline axial stresses

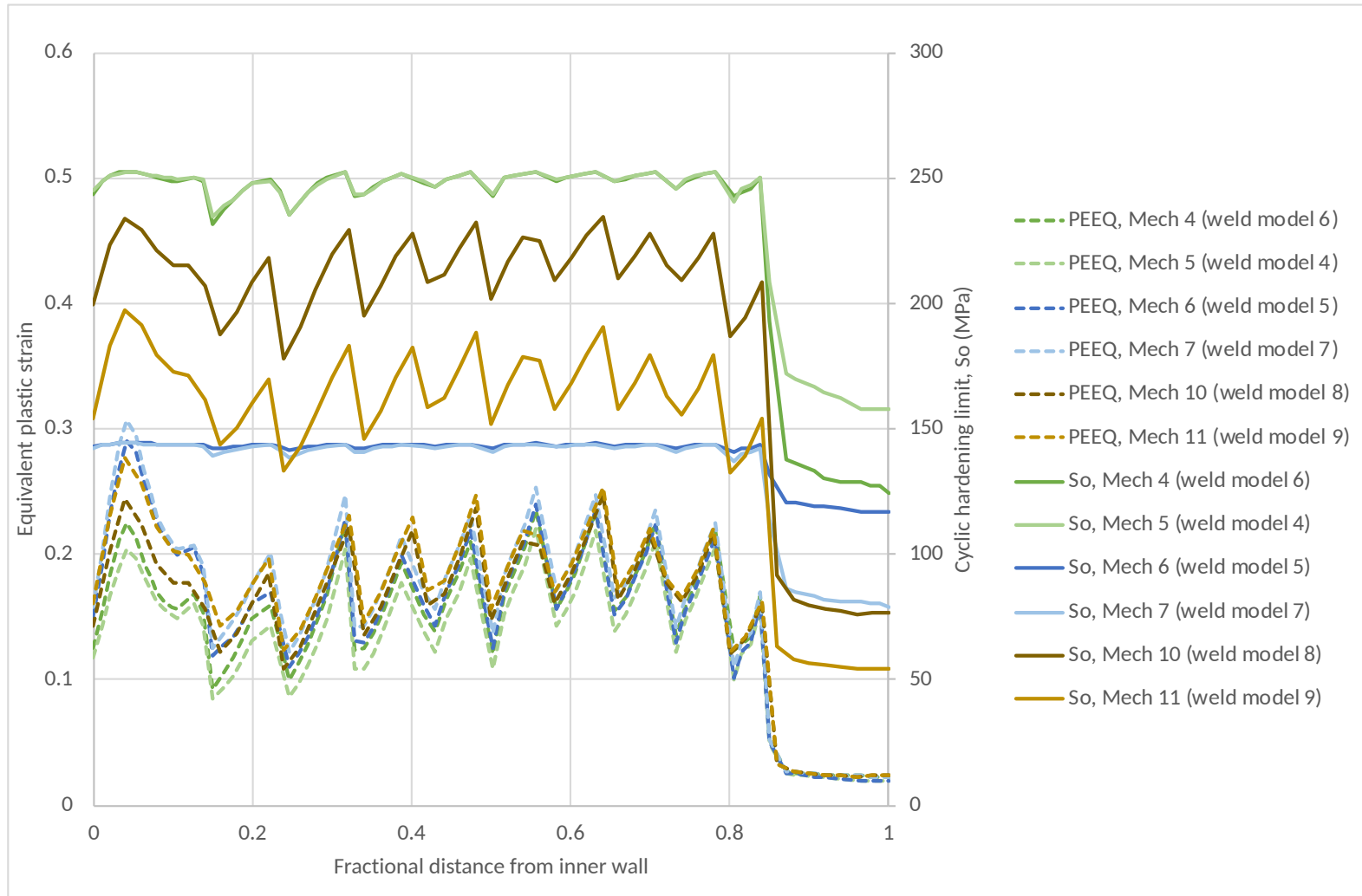


Figure 16: Through-wall distributions of equivalent plastic strain, PEEQ, and yield surface radius  $\sigma^0$ , on weld centreline, for mixed hardening analyses with different weld model parameters

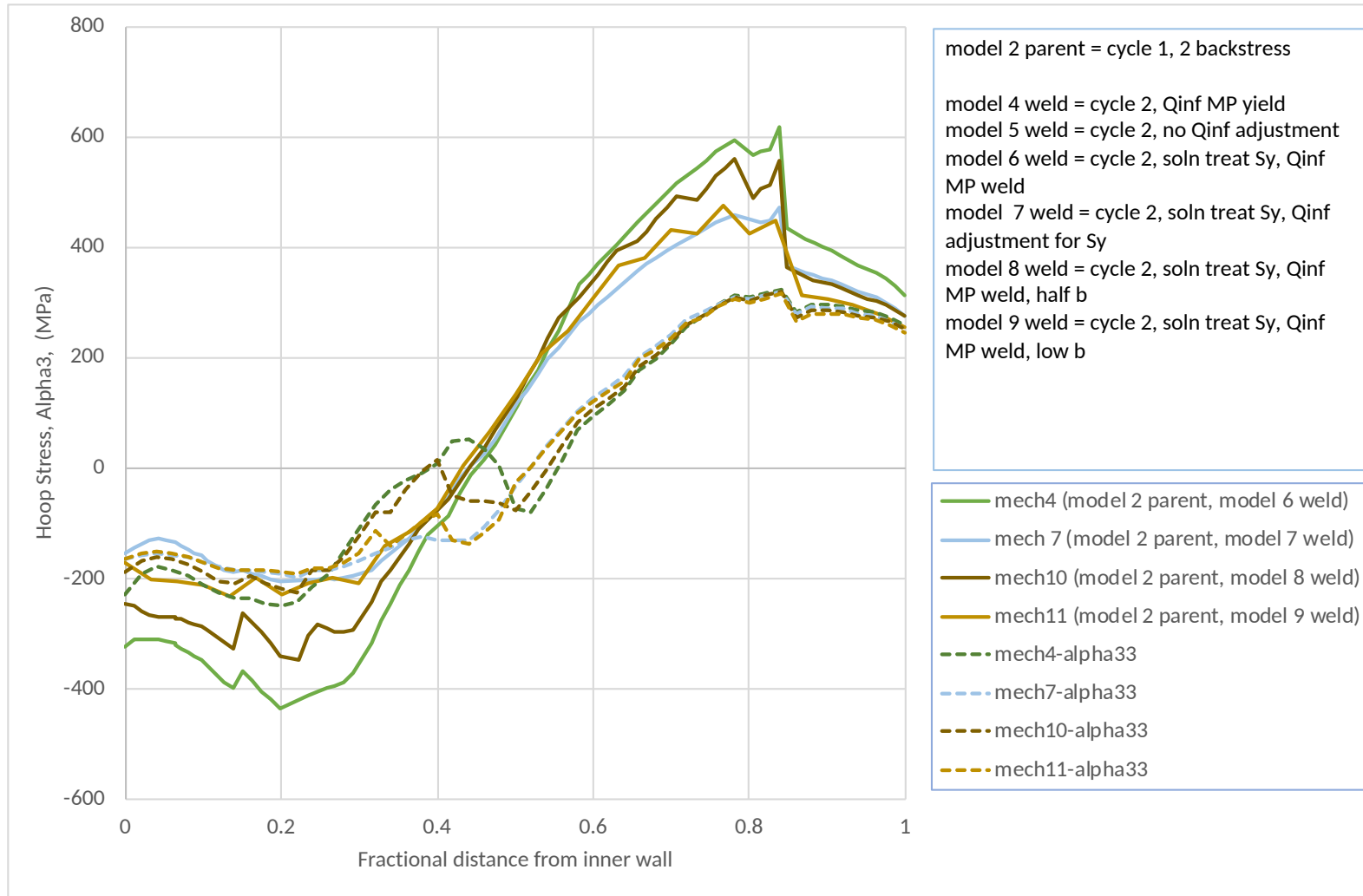


Figure 17: Showing the effect of weld metal starting yield strength and cyclic hardening behaviour on weld centreline hoop stresses, and back stress Alpha 33

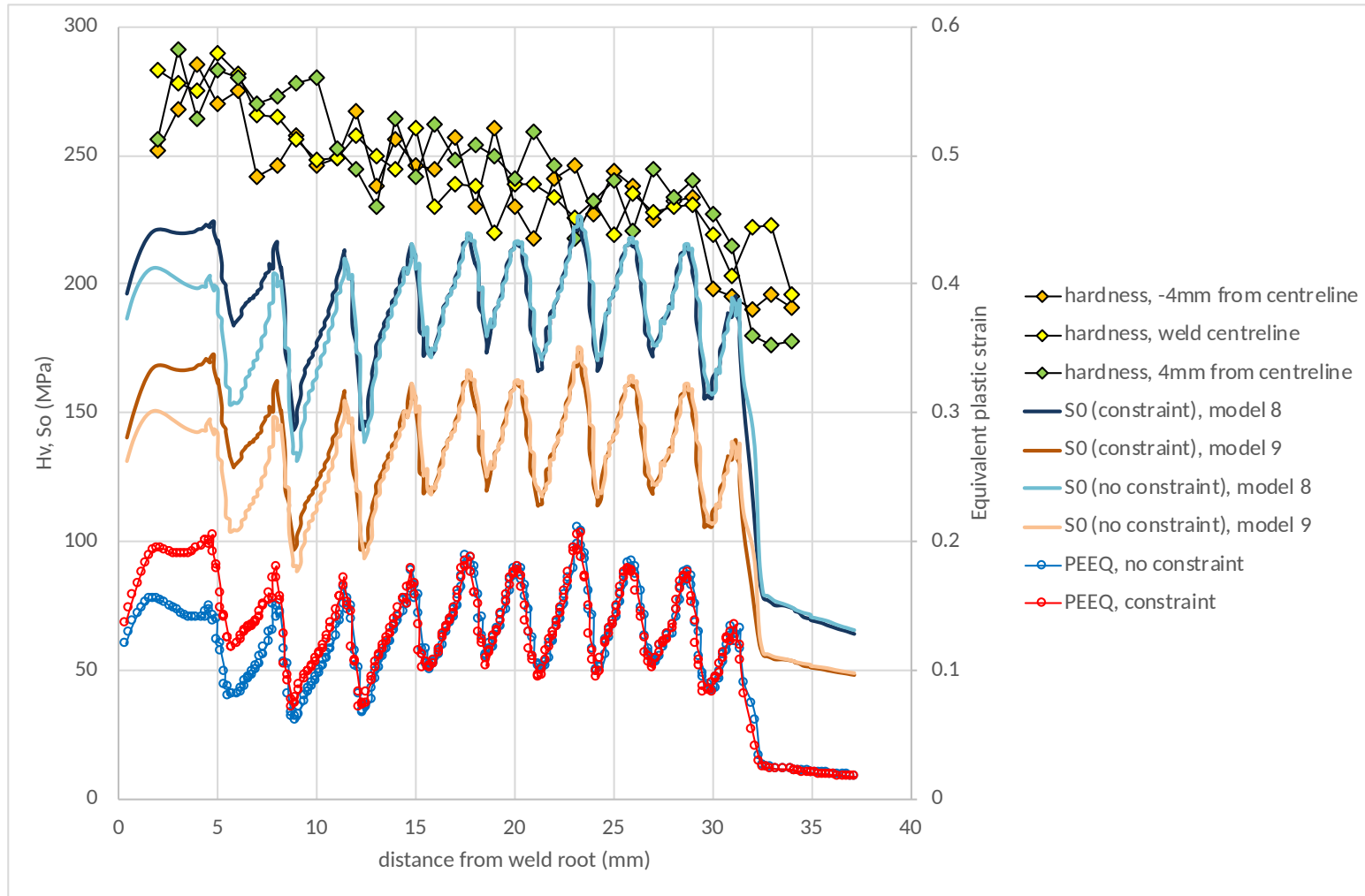


Figure 18: Showing the through wall variation of Vickers Hardness, equivalent plastic strain for two different axial restraint conditions, and inferred yield surface radius  $\sigma^0$  on the weld centreline

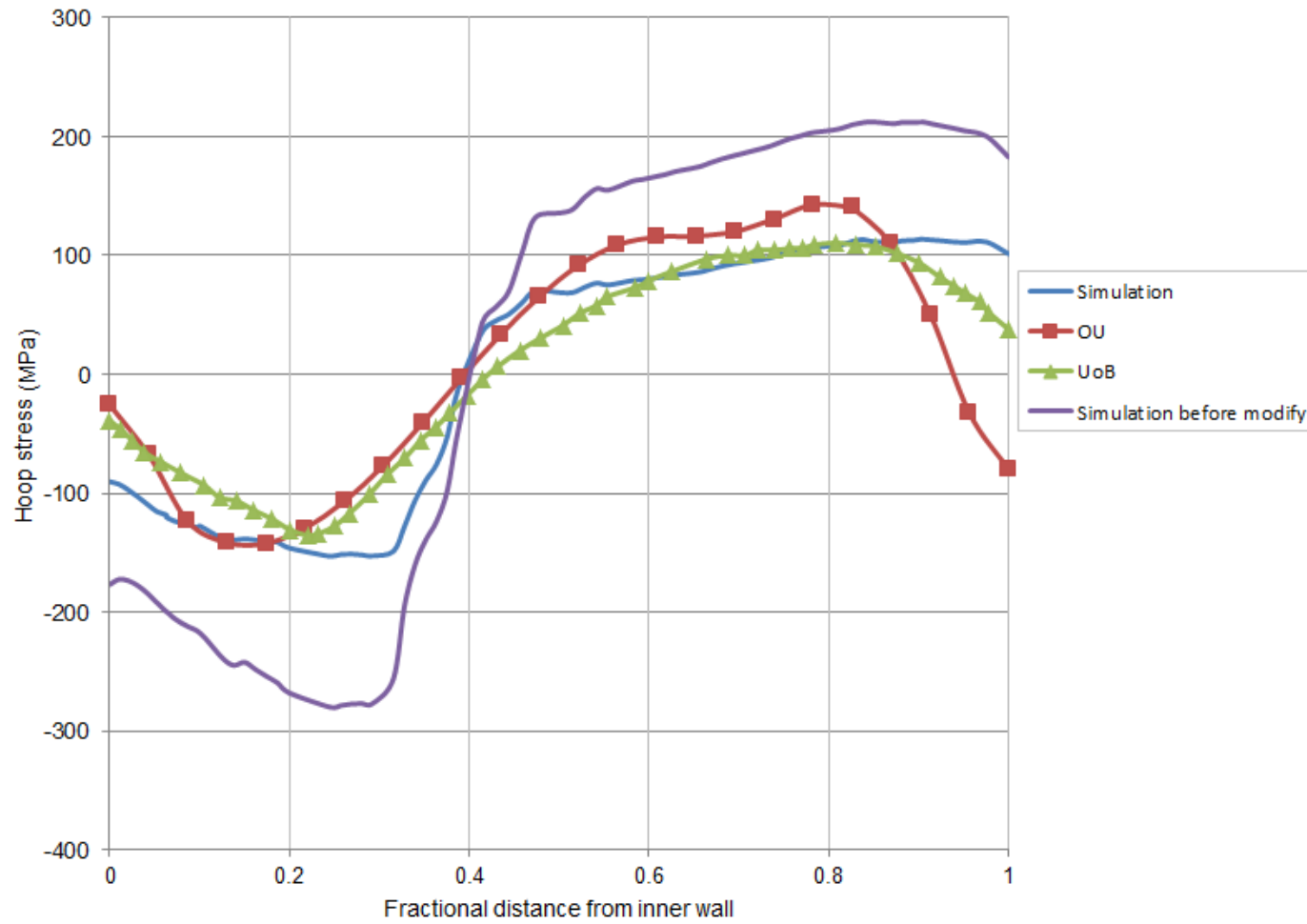


Figure 19: Comparing predicted and measured hoop stresses on the weld centreline after high temperature ageing

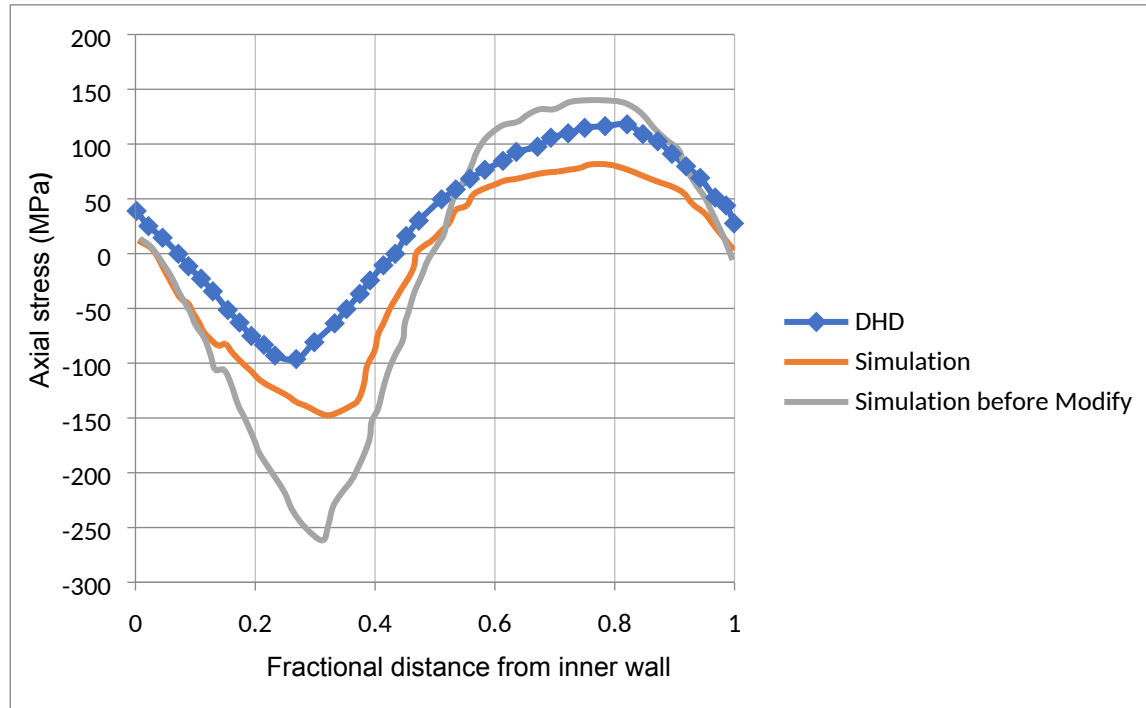


Figure 20: Comparing predicted and measured axial stresses on the weld centreline after high temperature ageing

